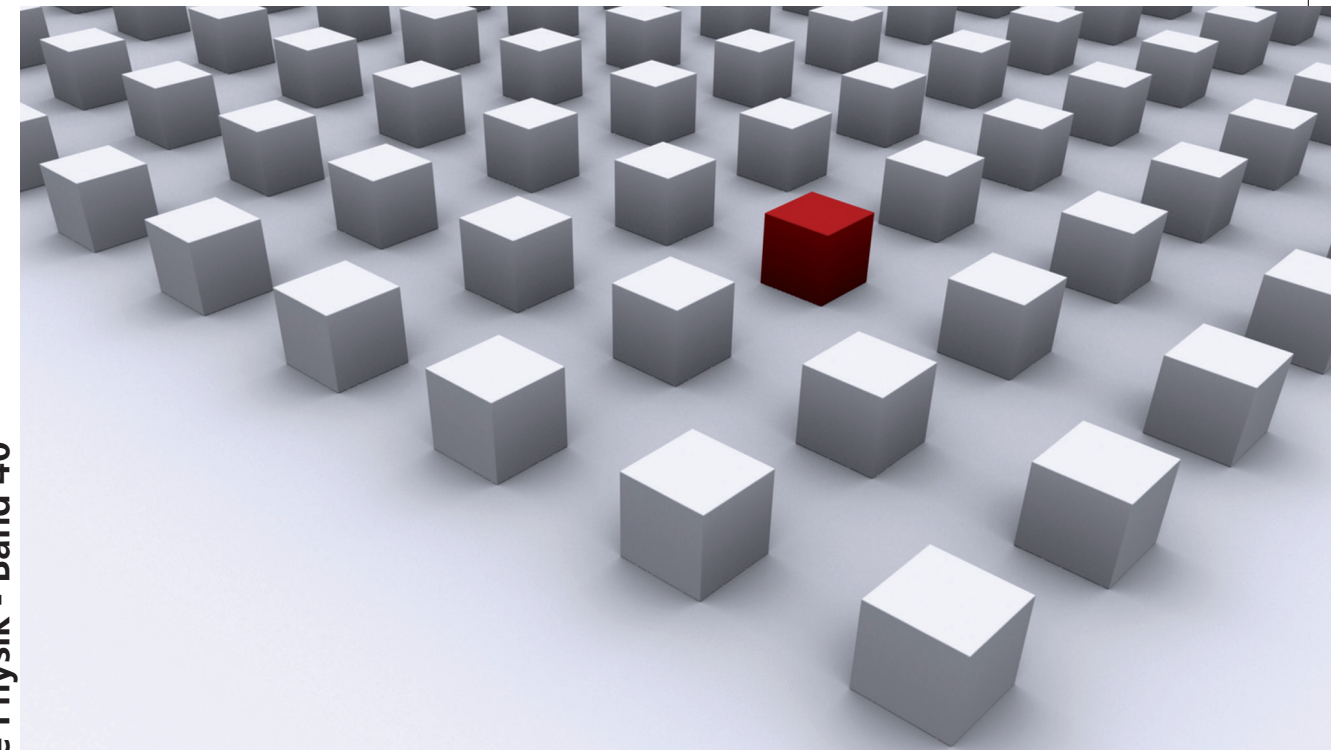


This work concentrates on scanning micro-Raman studies of nano-patterned singlelayer graphene. Graphene as a material is ideally suited for both electronics and spintronics, however for both applications nanopatterning is necessary. For graphene spintronics, pure zigzag edges are additionally required. It is therefore necessary to study the influence of nanopatterning and to verify attempts at creating pure zigzag edges.

To address the first issue, the work at hand comprises a Raman study of a series of samples of singlelayer graphene patterned with square antidot lattices. We have found this nanopatterned graphene to be p-type doped with the doping concentration tentatively depending on the number of antidots per square unit.

An attempt at creating pure zigzag edges has been made via an anisotropic etching process applied to square antidot lattices on singlelayer graphene. This thesis shows a step-by-step Raman evaluation of the etching process and verifies via inter-valley scattering that it indeed results in predominantly zigzag edges.

Disertationsreihe Physik - Band 40



Stefanie Heydrich

Raman spectroscopy of
nanopatterned graphene

Universitätsverlag Regensburg

Universitätsverlag Regensburg



ISBN 978-3-86845-110-8

gefördert von:



Universität Regensburg

Stefanie Heydrich

40

Disertationsreihe
Physik

Stefanie Heydrich



Raman spectroscopy of
nanopatterned graphene

Raman spectroscopy of nanopatterned graphene

Dissertation zur Erlangung des Doktorgrades der Naturwissenschaften (Dr. rer. nat.)
der naturwissenschaftlichen Fakultät II - Physik der Universität Regensburg
vorgelegt von

Stefanie Heydrich
aus Nürnberg
im Februar 2014

Die Arbeit wurde von Prof. Dr. Christian Schüller angeleitet.
Das Promotionsgesuch wurde am 12.02.2014 eingereicht.
Das Kolloquium fand am 03.06.2014 statt.

Prüfungsausschuss: Vorsitzender: Prof. Dr. V. Braun
1. Gutachter: Prof. Dr. C. Schüller
2. Gutachter: Prof. Dr. D. Weiss
weiterer Prüfer: Prof. Dr. S. Ganichev



Dissertationsreihe der Fakultät für Physik der Universität Regensburg, Band 40

Herausgegeben vom Präsidium des Alumnivereins der Physikalischen Fakultät:
Klaus Richter, Andreas Schäfer, Werner Wegscheider

Stefanie Heydrich

**Raman spectroscopy of
nanopatterned graphene**

Universitätsverlag Regensburg

Bibliografische Informationen der Deutschen Bibliothek.
Die Deutsche Bibliothek verzeichnet diese Publikation
in der Deutschen Nationalbibliografie. Detaillierte bibliografische Daten
sind im Internet über <http://dnb.ddb.de> abrufbar.

1. Auflage 2014
© 2014 Universitätsverlag, Regensburg
Leibnizstraße 13, 93055 Regensburg

Konzeption: Thomas Geiger
Umschlagentwurf: Franz Stadler, Designcooperative Nittenau eG
Layout: Stefanie Heydrich
Druck: Docupoint, Magdeburg
ISBN: 978-3-86845-110-8

Alle Rechte vorbehalten. Ohne ausdrückliche Genehmigung des Verlags ist es
nicht gestattet, dieses Buch oder Teile daraus auf fototechnischem oder
elektronischem Weg zu vervielfältigen.

Weitere Informationen zum Verlagsprogramm erhalten Sie unter:
www.univerlag-regensburg.de

Contents

| | |
|---|-----------|
| Contents | i |
| 1 Précis | 1 |
| 2 Motivation and Overview | 3 |
| 2.1 Graphene | 3 |
| 2.2 Raman spectroscopy | 5 |
| 2.3 Nanopatterning graphene: Antidots and zigzag edges | 6 |
| 3 Fundamental properties of graphene and Raman scattering in graphene | 9 |
| 3.1 Fundamentals of Raman scattering | 9 |
| 3.2 Graphene - crystal lattice, band structure and phonon dispersion . | 11 |
| 3.2.1 Crystal lattice of graphene and stacking order of multilayer graphene | 11 |
| 3.2.2 Electronic bands and phonon dispersion | 13 |
| 3.3 Raman scattering in graphene | 16 |
| 3.3.1 Raman modes in graphene | 16 |
| 3.3.2 Influence of the number of layers on the 2D mode | 21 |
| 3.3.3 Influence of edge chirality on the D mode | 22 |
| 3.3.4 Influence of charge carriers on the G and 2D modes | 24 |
| 4 Sample fabrication and experimental setup | 27 |
| 4.1 Sample fabrication and samples | 27 |
| 4.1.1 General preparation of single layer graphene and substrate | 27 |
| 4.1.2 Single layer graphene with backgate | 28 |
| 4.1.3 Single layer graphene with circular antidots | 28 |
| 4.1.4 Single layer graphene with hexagonal antidots | 31 |
| 4.2 Experimental setup | 33 |
| 5 Experimental results | 35 |

| | | |
|----------|--|-----------|
| 5.1 | Basic information to scanning Raman spectroscopy in graphene . . . | 35 |
| 5.2 | G peak position and lineshape in single layer graphene with backgate | 39 |
| 5.3 | P-type doping in single layer graphene with circular antidots . . . | 43 |
| 5.4 | Raman study of anisotropically etched hexagonal antidots in single layer graphene | 49 |
| 6 | Conclusion and outlook | 59 |
| 6.1 | Conclusion | 59 |
| 6.2 | Outlook | 60 |
| | Bibliography | 61 |

Chapter 1

Précis

Graphene is valued for its high charge-carrier mobility, its flexibility and transparency, its ability to withstand mechanical stress, and, not least, the fact that it is a two-dimensional material, whose existence was predicted to be forbidden by theory [Pei35] [Lan37]. Due to these properties, graphene readily lends itself to many applications in electronics, opto-electronics, sensing, the construction of heterostructures with other two-dimensional materials, and many other fields. One hope for the future is that graphene may succeed silicon as base material for electronics, as silicon-based electronics will very soon reach their performance limit and graphene is among the best alternatives. However, graphene has no intrinsic band gap, which severely hurts the construction of graphene field-effect transistors and generally the transfer of Si-based electronics to graphene-based electronics. Several ways have been found to successfully address this issue, among them the periodic patterning of graphene with antidots, which opens a band gap. However, the effect of nanopatterning on graphene has not been studied in depth.

Theorists have predicted a spin-polarized edge state in graphene along perfect zigzag edges, making graphene a material perfect for spintronic applications. However, graphene flakes with perfect zigzag edges have not yet been realized, removing the possibility of graphene spintronics even further into the future than the hope for graphene electronics.

This work will concentrate on the effect of nanopatterning realized through periodic antidot lattices in graphene and the preparation of predominantly zigzag edges. We have prepared a series of samples of single layer graphene flakes with square antidot lattices with different lattice constants ranging from 80 nm to 400 nm and two sizes of antidot diameters (50 nm and 60 nm). Scanning Raman spectroscopy on patterned samples showed an increase of the D peak intensity and a decrease of the G peak intensity as well as stiffening, that is an up-shift of the G mode position. The former two are due to artificial introduction of defects

and decrease of graphene per unit area by the antidots, respectively, while we attribute the latter to doping. Through careful evaluation of the positions of G and 2D modes, we have determined the graphene antidot lattices to be p-type doped with charge carrier concentrations ranging from $3 \times 10^{12} \text{ cm}^{-2}$ in the 400-nm sample to $7 \times 10^{12} \text{ cm}^{-2}$ in the 80-nm sample.

Additionally, we have studied the preparation process of a large single layer graphene flake patterned with two types of square antidot lattices with 200 nm and 400 nm lattice constant, respectively, that have predominantly zigzag edges resulting from anisotropic etching. This flake is in contrast to graphene flakes with usual antidots, whose edges contain both zigzag and armchair edge configurations in comparable amounts. The flake was processed in five steps - exfoliation from natural graphite (1), patterning of conventional antidots via electron beam lithography and reactive ion etching (2), a preparation step (3), and two successive anisotropic etching steps (5). Only one anisotropic etching step is necessary; we added another to see, if prolonged etching increases the ratio of zigzag to armchair edges. After each step, we performed two Raman scans, one monitoring the D and G peak and one monitoring the 2D peak. Since the D peak probes intervalley scattering, which is forbidden for pure zigzag edges, we evaluated the D peak intensity for each step and have found the antidot edges to be predominantly zigzag after the anisotropic etching. Two anisotropic etching steps were performed to see if continued etching would increase the zigzag-to-armchair ratio and we have found this to be the case.

We have also determined doping after each preparation step in the area where the 200 nm antidot lattice was etched and have found the flake to be p-type doped after every step like the conventional, circular antidots, ranging from $4.5 \times 10^{12} \text{ cm}^{-2}$ after the preconditioning step to $9 \times 10^{12} \text{ cm}^{-2}$ after the final anisotropic etching step.

Chapter 2

Motivation and Overview

This chapter is designed to give an overview of the field this work is associated with. We will first discuss prior research on graphene, its properties, and applications, insofar as they have been realised, and areas where information is still scarce. We will then introduce the merit of Raman spectroscopy as an investigative tool, highlighting its role in graphene research. Thirdly, the concept of antidots will be introduced. We will summarize their effects on graphene, as they have been discussed in literature. Lastly, we will name some advantages gained by being able to fabricate graphene devices with defined edge-chiralities. We will finish by embedding the research presented in this work into the context of state-of-the-art graphene research.

2.1 Graphene

This section introduces the material graphene in general terms, touching on its many desirable qualities and noting several areas where graphene is a promising candidate, like optoelectronics, electronics, and heterostructures, and the progress in research and development achieved there.

Graphene is a two-dimensional carbon allotrope and, after sixty years of theoretical study [Wal47] [Tia94] [Nak96] [Woo00] [Gon01] [Rei02], the first quasi-freestanding two-dimensional solid to have been isolated [Nov04]. Fundamental research favors graphene obtained by the so-called mechanical cleaving method first described in 2004 [Nov04], which has since been refined [Nov05], because it produces mostly clean, unstrained graphene. However, flakes are small, ranging from a few to a few 100 μm in size, randomly deposited on a substrate. For many applications, production methods like chemical vapor deposition (CVD) [Li09]

and epitaxial growth on SiC [Ber06] [Oht06] are preferable, since they yield large flakes, in the range of several tens of inches [Bae12]. Graphene has also been synthesized using liquid-phase exfoliation [Her08].

The development of different isolation methods allowed, after years of theoretical exploration only, experimental research into graphene's many exciting properties. It is two-dimensional, it is extremely stiff, yet strong and elastic, it conducts both heat and electric current exceptionally well, it is transparent. These qualities make graphene an ideal candidate for a number of applications and, understandably, research is intense.

In electronics, for example, graphene is valued for its conductive capabilities and flexibility. It can be used to realize flexible electrodes in organic light emitting diodes (OLEDs) [Han12] and solar cells [Wan08]. Since it is also transparent, it has been used as transparent electrode in a touch-screen [Bae12]. Its high carrier-mobility is invaluable in high-frequency transistors [Lia10] [Wu10] [Lin11], exceeding state-of-the-art silicon transistors of the same gate length [Lin10a]. However, pristine graphene has no band gap, which prohibits switching off in field effect transistors, so many attempts have been made to open a - preferably continuously scalable - band gap while maintaining the excellent transport properties. One scheme is through quantum confinement in graphene nanoribbons (GNR) [Son06a] [Han07], however, the size of the gap is very sensitive to ribbon width and the atomic configuration of the edge, and narrow ribbons are incapable of carrying large currents. Other attempts are substrate- [Hic13] [Zho07] or strain-induced [Ni08b] [Gui10] bandgaps; the first is not tunable and the tunability of the latter is limited by the amount of strain the graphene can take without breaking. The most promising candidate to open a bandgap in graphene is nanopatterning, by hydrogen passivation [Bal10], boron or nitrogen doping [Ci10], and antidots [Ero09]. The latter will be discussed in more detail below.

Graphene is also a promising candidate for opto-electronics. It can be turned into a photodetector [Xia09] or a solar cell [Mia12]. It can be used as a saturable absorber in mode-locked lasers [Sun10] with ultrawideband tunability [Zha10] or in passively Q-switched lasers [Pop11].

Another possible application for graphene is in the fields of sensors [Koc12] and bio-sensors [Kui11].

Preparation of graphene has also spawned research into other two-dimensional materials like boron nitride (BN) [Nov05], NbSe₂ [Nov05] [Col11], TaSe₂ [Col11] and molybdenite (MoS₂) [Nov05] [Mak10] [Kor11] [Rad11] [Ple12b] [Ple12a]. Combinations of these materials lead to heterostructures, which can e.g. be made into high-frequency transistors [Bri12].

Graphene may also be used as a substrate. In transmission electron microscopy (TEM) [Nai10], molecules are placed on a graphene single layer, which is draped over a hole in the sample holder. In Raman spectroscopy, molecules on graphene exhibit an enhanced signal compared to the conventional substrate SiO₂ [Lin10b] and a frequency shift [Yag12]. This is called graphene-enhanced Raman scattering

(GERS).

2.2 Raman spectroscopy

This section concentrates on the merits of Raman spectroscopy as an investigative tool in general and its advantages when used to analyze graphene in particular. Raman scattering is an inelastic scattering process of a photon creating or annihilating an excitation in the probed material. Comparing the energy of incoming and scattered photon yields information about allowed excitations in the material. In 1928, C. V. Raman and K. S. Krishnan observed the Raman effect in liquids [Ram28], and G. Landsberg and L. I. Mandelstam in crystals [Lan28]. It had been predicted theoretically in 1923 by A. Smekal [Sme23] to probe vibrational, rotational and other, low-frequency modes in a system, giving information about the intrinsic make-up of the sample. The fact that it is very fast and non-destructive and can, when combined with a microscope, be used to probe samples with sub- μm resolution makes it a very attractive method.

Therefore, Raman spectroscopy is frequently used to analyze both liquid samples and crystals. In chemistry and biology, liquid samples are probed most commonly to gain specific knowledge about chemical bonds and symmetries in molecules, resulting in a Raman fingerprint for each specific molecule. In solid-state physics, crystals are probed to learn about their phonon dispersion, to measure temperature and to determine the crystallographic orientation.

In graphene, Raman spectroscopy has been used to probe the phonon dispersion [Rei04]. It can determine the number of layers in few-layer samples [Fer06] by sounding the electronic structure in the sample, which evolves with the number of layers. The Raman spectrum in single layer graphene changes with doping [Yan07] [Pis07] [Das08], making it possible to determine charge carrier densities via Raman spectroscopy [Hey10]. Uniaxial [Ni08b] and biaxial [Met10] strain in graphene single layers leave fingerprints in the Raman spectrum. Already in 1970, the effects of grain boundaries in nanocrystallite graphite on the Raman spectrum have been studied [Tui70]. After the discovery of graphene, this research was extended to graphene, researching both different kinds of defects and concentrations of defects using Raman scattering [Cas07] [Cas09a] [Can11] [Eck12]. Scanning Raman spectroscopy can not only give single spectra at one position on a sample, but image the topology of a flake. This can be used to determine the edge chirality and, ultimately, the crystal orientation [You08] [Cas09b] of a given flake.

2.3 Nanopatterning graphene: Antidots and zigzag edges

The first part of this section introduces the concept of antidots and covers their part in graphene research. The second part concentrates on the possibility of graphene devices with perfect zigzag edges being used to realize spintronics and the experimental progress made in this direction.

An antidot lattice is an array of holes etched into the sample, designed to superimpose a periodic potential landscape on the sample. Antidots can be arrayed in rows and columns with equal distances and are then called a square lattice, or in a hexagonal, or a triangular fashion. Antidots were first introduced in GaAs-AlGaAs heterojunctions as a square array of microscopic holes etched into a high-mobility 2DEG conductor, where anomalous low-field Hall plateaus and a quenching of the Hall effect about $B=0$ were observed [Wei91]. Weiss et al. calculated that the antidots interrupt classical commensurate orbits of charge carriers, causing the observed effects. Later, quantum oscillations in magnetotransport in similar samples were reported [Wei94].

Graphene patterned with an antidot lattice exhibits prominent absorption resonances in the microwave and terahertz regions due to surface plasmons in the graphene disturbed by the superlattice [Nik12]. Recently, coupling of such plasmons in graphene antidot lattices to substrate phonons has been observed experimentally and described theoretically [Zhu13].

As already mentioned above in the section on graphene, imposing a superstructure via antidot lattices leads to the opening of a bandgap in graphene in the range of several meV [Ero09] [Pet11]. Different lattice types, square, hexagonal, or triangular, create larger or smaller band gaps [Ouy11]. The position of the individual antidots with respect to the underlying graphene lattice also influences the size of the gap [Dvo13].

Etching antidot lattices into graphene also introduces p-type doping in the flake [Hey10] [Beg11]. In both cases, Raman spectroscopy was employed to quantify the amount of doping.

Manipulating a graphene antidot lattice by leaving out some of the antidots creates defect states or pairs of coupled defect states in the antidot lattice, which can function as hosts for electron spin qubits [Ped08].

Owing to its honeycomb-like atomic structure, graphene can have two types of ordered edges: so-called armchair and so-called zigzag edges. (See chapter 3 for more information on edge chirality.) Along a pure zigzag edge, an exceptionally large local electron density and a spin polarized edge state were predicted [Son06b] [Wim08] [Yaz08], making graphene the perfect material for spintronic applications. So far, edge states have been detected using e.g. STM to investigate graphene nanoribbons [Zha13], but spin polarized edge states have only been proposed in theory. Production of perfect zigzag edges is still a great challenge

and so far, no devices have been realized. It has been possible, however, to etch antidots with dominating zigzag edges [Kra10] [Obe13]. In both cases, Raman spectroscopy was used to determine the edge chirality. In the latter, weak localization was additionally employed.

Chapter 3

Fundamental properties of graphene and Raman scattering in graphene

In this chapter, both graphene and Raman scattering will be introduced. The chapter begins with a short, basic introduction into Raman scattering in general, highlighting resonant and double-resonant Raman processes. In the second part, we will discuss single-, bi-, and multilayer graphene and graphite in terms of its atomic configuration and the resulting electron and phonon dispersions. The most prominent Raman modes in graphene will be briefly introduced. In the last part of this chapter, all Raman modes in graphene examined in the experimental part of this work, namely the G, D, D' and 2D peaks, will be discussed in depth. This discussion will include the influence of the number of layers in a sample, charge carriers, and edge chirality on certain peaks.

3.1 Fundamentals of Raman scattering

Raman scattering (sometimes also called **combination scattering**) is an inelastic scattering process of light on a medium, creating or annihilating an excitation in the material. The scattering process is then called Stokes or Anti-Stokes process, respectively, as depicted in Fig. 3.1(a) and (b). In both cases, **energy conservation**

$$\hbar\omega_1 = \hbar\omega_2 \pm \hbar\omega_{ex} \quad (3.1)$$

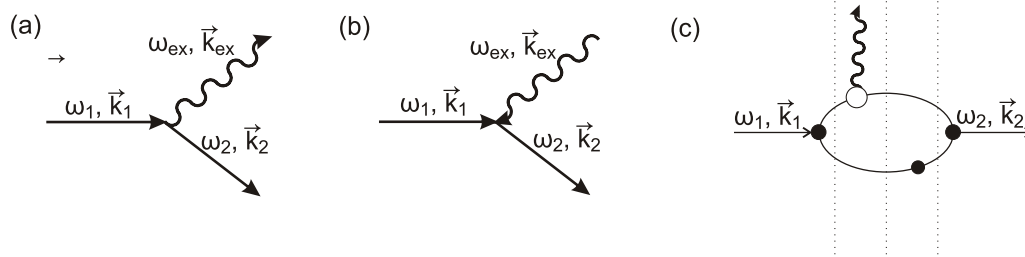


Figure 3.1: Feynman diagram for a (a) Stokes and (b) Anti-Stokes scattering process. The solid straight lines indicate photons, the wavy line depicts the excitation in the material. (c) Feynman diagram for a second-order Raman process. The incoming light creates an electron-hole pair, the electron is scattered by a phonon (white circle), the hole is then scattered by a defect (black circle) before electron and hole recombine. The vertical dashed lines indicate intermediate states.

where ω_1 denotes the frequency of the incoming photon, ω_2 the frequency of the scattered photon and $\hbar\omega_{ex}$ the energy of the created or annihilated excitation, and **momentum conservation**

$$\hbar\vec{k}_1 = \hbar\vec{k}_2 \pm \hbar\vec{q} + \hbar\vec{K} \quad (3.2)$$

with \vec{k}_1 denoting the k -vector of the incoming photon, \vec{k}_2 the k -vector of the scattered photon, \vec{q} the k -vector of the excitation and \vec{K} a vector of the reciprocal lattice, must be fulfilled. For the purposes of this work, the incoming photon creates an electron-hole pair and the excitation is always a phonon.

Since typical experiments are conducted using light sources in the 1064 - 229 nm range and the lattice parameter a is of the order of a few Å, (≈ 2.46 Å in graphene), $k_1, k_2 \ll \pi/a$ (see e.g. supplementary information of [Fer13]). Then follows from eq. 3.2, that the phonon wave vector $q \approx 0$ in first-order scattering. This is dubbed the **fundamental Raman selection rule**. In first order, only scattering processes involving a phonon near Γ are **Raman-allowed**. Scattering processes involving only one phonon with large k -vector are **Raman-forbidden** and require a defect for momentum conservation. One example is shown in Fig.3.1(c). Therefore, such scattering processes can only take place at defect sites, never in the perfect crystal. The emission (or absorption) of two phonons, however, can always satisfy eq. 3.2: $q + (-q) = 0$.

The intensity of a Raman peak is contingent on the **differential scattering cross section** $d\sigma$ for the Raman scattering of an initial photon (\vec{k}_1, ω_1) into the solid angle $d\Omega$ which in turn depends on the matrix elements $K_{2f,10}$ as (see e.g. (3.6) of [Mar83])

$$d\sigma(\vec{k}_1\omega_1) = |K_{2f,10}|^2 (\hbar\omega_1 - E_f)^2 d\Omega / (4\pi^2 \hbar^4 c^4) \quad (3.3)$$

when E_f denotes the final energy of the system.

Since Raman scattering is a scattering process of light on a medium, its cross

section depends on the interaction between radiation and matter, described by the radiation-matter-interaction Hamiltonian \mathcal{H}_{RM} . $K_{2f,10}$ describes the matrix elements which contribute to the scattering cross-section. The indices 0, f of $K_{2f,10}$ refer to the ground and final phononic state, respectively, the indices 1, 2 denote the incoming and outgoing photon.

For a first order process, the matrix elements $K_{2f,10}$ can be expressed in second order perturbation theory as ((3.31) in [Mar83])

$$K_{2f,10} = \sum_{i,j} \frac{M_{fj}\mathcal{M}_{ji}M_{i0}}{\hbar^2(\omega_1 - \omega_i - i\gamma_i)(\omega_1 - \omega_j - i\gamma_j)} \quad (3.4)$$

when $M_{fj} \equiv \langle f|\mathcal{H}_{RM}|j \rangle$ and $M_{i0} \equiv \langle i|\mathcal{H}_{RM}|0 \rangle$ denote the constant matrix elements of the radiation-matter-interaction, $\mathcal{M}_{ji} \equiv \langle j|\mathcal{H}_{ep}|i \rangle$ denotes the matrix element of the electron-phonon-interaction with \mathcal{H}_{ep} the Hamiltonian describing the electron-phonon interaction, and γ_i is the broadening parameter.

For an n -phonon process, eq. 3.4 can be expanded to [Mar83]

$$K_{2f,10} = \sum_{s_0, \dots, s_n} \frac{M_{fs_0}\mathcal{M}_{s_0s_1}\dots\mathcal{M}_{s_{n-1}s_n}M_{s_n0}}{\hbar^{n+1}(\omega_1 - \omega_{s_0} - i\gamma_{s_0})(\omega_1 - \omega_{s_1} - i\gamma_{s_1})\dots(\omega_1 - \omega_{s_{n-1}} - i\gamma_{s_{n-1}})(\omega_1 - \omega_{s_n} - i\gamma_{s_n})}. \quad (3.5)$$

Typically, all intermediate energy states involved in a Raman scattering process are virtual. Since the scattering process happens on a very short timescale, the **uncertainty principle**

$$\Delta E \Delta t \geq \frac{\hbar}{2} \quad (3.6)$$

where ΔE is the energy difference from the virtual state to the next eigenstate and Δt is the lifetime of the virtual state, allows the violation of energy conservation for intermediate states. This does not affect energy conservation of the overall process.

However, if one intermediate state is an eigenstate of the material, the scattering process is called **resonant** and eq. 3.5 diverges. If, in a higher order process, two (three) intermediate states are real, this is called a **double (triple) resonance**.

3.2 Graphene - crystal lattice, band structure and phonon dispersion

3.2.1 Crystal lattice of graphene and stacking order of multilayer graphene

single layer Graphene is a two-dimensional material made of sp^2 -hybridized carbon atoms. Each carbon atom is covalently bound to its three neighboring

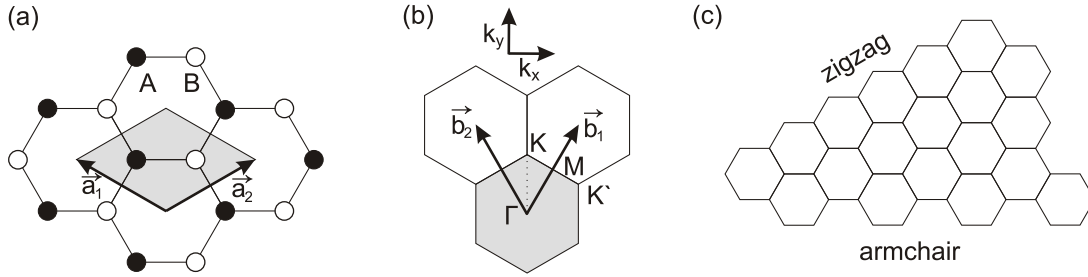


Figure 3.2: (a) real space representation of graphene. The lattice is spanned by two basis vectors \vec{a}_1 , \vec{a}_2 framing the rhombic unit cell, shaded light gray. Black and white circles denote carbon atoms of the two sublattices. (b) reciprocal space. The shaded hexagon represents the first Brillouin-zone, \vec{b}_1 and \vec{b}_2 denote the primitive vectors and K , K' and M mark points of high symmetry. k_x and k_y identify the coordinate axes in reciprocal space. (c) real space representation of the graphene lattice exhibiting a zigzag and an armchair edge.

atoms. The crystal structure consists of a rhombic unit cell, with two inequivalent base atoms A and B, spanned by base vectors \vec{a}_1 and \vec{a}_2 with lattice constant $|\vec{a}_1| = |\vec{a}_2| = 2.461 \text{ \AA}$. The distance between neighboring carbon atoms is $a_{C-C} = 1.42 \text{ \AA}$. This array results in the well-known honeycomb lattice with two sublattices A and B as may be seen in Fig. 3.2(a). In reciprocal space, the first Brillouin zone is a honeycomb with corners denoted K and K' , since they are not connected by primitive vectors of the reciprocal lattice \vec{b}_1 and \vec{b}_2 and thus inequivalent, see Fig. 3.2(b). The edge of a graphene flake is typically made up of a combination of two atomic configurations called **zigzag** and **armchair**, shown in Fig. 3.2(c). single layer graphene consists of only one carbon layer, in **bilayer graphene**, two single layers are stacked on top of each other, following the **A-B Bernal stacking** with an interlayer distance of 3.35 \AA . Bernal stacking means that the top layer is shifted rigidly in-plane by a_{C-C} with respect to the bottom layer so that all atoms of sublattice A in the top layer lie over atoms of sublattice B in the bottom layer. All atoms in sublattice B of the top layer have no carbon atoms directly underneath in the bottom layer. Bilayer graphene exfoliated from graphite will follow this stacking order.

It is also possible to find two layers of graphene not following the Bernal stacking. Epitaxially grown graphene may consist of two or more rotated layers, exhibiting a fingerprint Moiré pattern in STM images [Pon05]. This is called twisted graphene and its electronic properties differ from those of bilayer graphene [Li10a]. Another kind of two-layer graphene is folded graphene. It is created artificially from single layer graphene flakes on SiO_2 by flushing acetone or other liquids over the sample, folding part of a flake back in on itself or by growing graphene through chemical vapor deposition (CVD) on specially prepared copper foils. The latter method

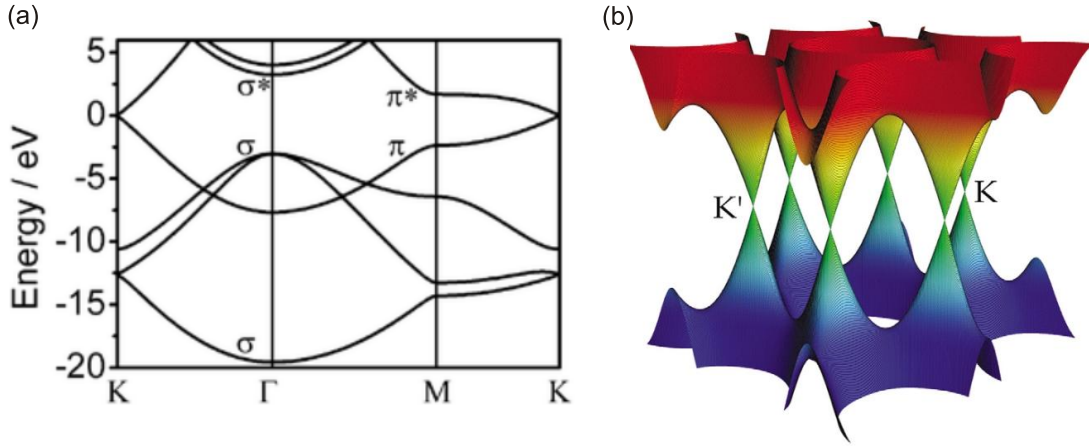


Figure 3.3: (a) two-dimensional band structure of graphene depicting both the π and the σ bands. The π and π^* bands cross at the Fermi level, forming valence and conduction band. Image from [Li10b] (b) three-dimensional image of the graphene valence and conduction band, obtained through tight-binding calculations. The π and π^* bands are linear around K and almost mirror each other. Image from [Kat07].

allows position control of the fold [Kim11]. In both cases, the folding influences the electronic properties of the graphene, e.g. reducing the Fermi velocity [Ni08a]. **Multilayer graphene** consists of three or a few more layers and can be stacked following either an A-B-A-B or an A-B-C stacking sequence where the third layer is shifted rigidly in-plane with respect to the second layer by a_{C-C} like the second layer is to the first. Both stacking orders may be found in natural graphite, but A-B-A-B Bernal stacking is much more common than A-B-C stacking. In this work, we will limit ourselves to A-B-A-B Bernal stacked samples.

3.2.2 Electronic bands and phonon dispersion

Graphene is often called a semi-metal or a gapless semiconductor. The reason for this is evident from graphene's **bandstructure**, shown in Fig. 3.3. As mentioned above, graphene consists of sp^2 -hybridized carbon atoms, each of which is covalently bound to three neighboring atoms. The p_z orbitals form the π valence and π^* conduction band, which cross at the Fermi level at the K and K' points, also called Dirac points in the context of electronic bands. The Fermi surface of graphene therefore consists of 6 points, only two of which are geometrically inequivalent. In the vicinity of the Dirac point, both valence and conduction band are linear and almost mirror each other, inducing many of graphene's characteristic qualities. Fig. 3.3(a) shows a two-dimensional representation of both the π and the σ bands, formed by the in-plane bonds of graphene. The energy gap

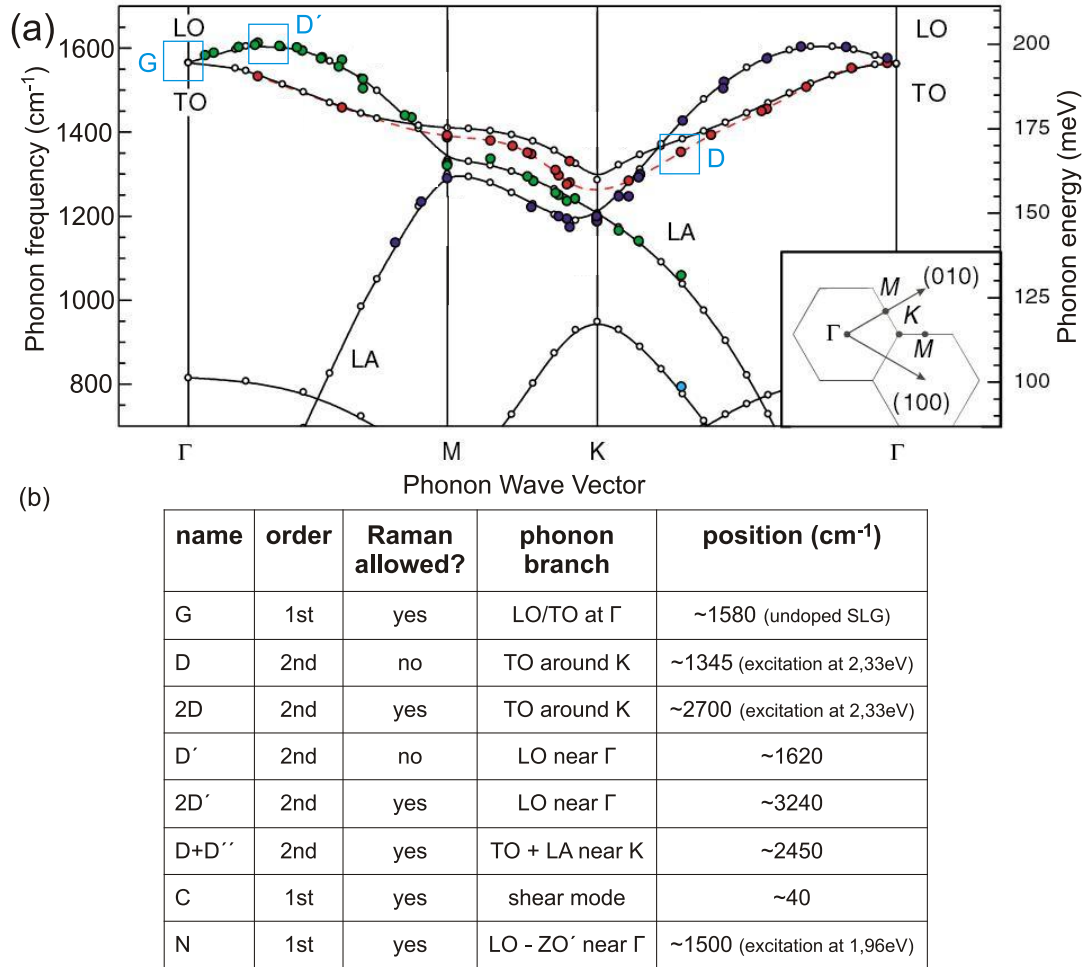


Figure 3.4: (a) phonon dispersion of graphite (adapted from [Mau04b]). Solid lines are *ab initio* calculations, filled circles are experimental data gathered by inelastic x-ray scattering, the dashed red line is a cubic spline connecting the experimental data for the TO branch. The light blue squares mark the phonon branches contributing most to the indicated peak. Inset: Brillouin zone of graphene with high-symmetry points Γ , K , and M . (b) table of most prominent Raman features in graphene and graphite. Listed are the name most common in literature, order of the Raman process, whether the scattering process is Raman allowed, the involved phonon branch(es), and the position of the mode in the spectrum.

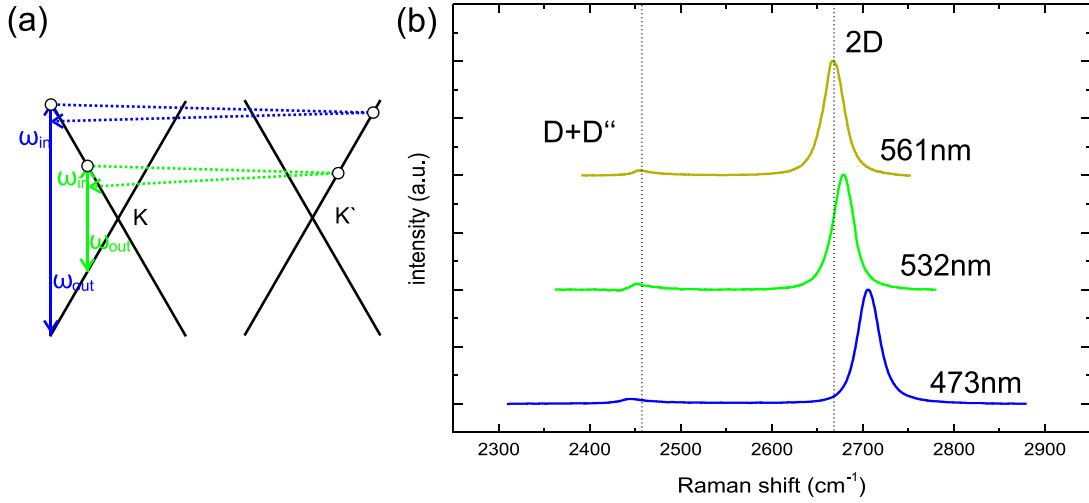


Figure 3.5: (a) schematic of two double-resonant scattering processes with different excitation energies. The resonance condition necessitates different phonon k -vectors for different laser energies. (b) $D+D''$ peak and $2D$ peak in graphene measured with 473 nm, 532 nm, and 561 nm excitation wavelength. Both shift position if the excitation wavelength is changed.

between the σ bands is very large and they are far away in energy (of the order of tens of eV) from the Fermi point. Therefore, the valence- and conduction bands are formed by the π and π^* bands around K. A three-dimensional diagram of graphene's π bands is shown in Fig. 3.3(b), where their similarity and linearity around the K points is particularly striking. For a theoretical discussion of the electron dispersion, see e.g. [Wal47],[Slo58] and [Par06].

Fig. 3.4(a) shows the **phonon dispersion** of graphite, obtained by *ab initio* calculations (solid lines) and corroborated by experimental data garnered by x-ray scattering (colored dots)[Mau04b]. The in-plane optical phonons are degenerate at the Brillouin-zone center and softened by a **Kohn anomaly**, as is the transversal-optical (TO) phonon at the K point [Pis04]. A Kohn anomaly is a softening of phonons in metals caused by electrons screening the lattice vibrations and coupled to k_F . Therefore, the shape of the Fermi surface determines, where such a kink in the phonon dispersion appears. The Fermi surface of graphene consists of six points connected by the vector \vec{K} and a Kohn anomaly may consequently only be found at Γ and K [Koh59][Pis04]. For a more detailed discussion of the phonon dispersion, see e.g. [Sai02], [Mau04a] and [Mau04b].

Fig. 3.4 (b) shows an overview of the most prominent Raman modes in graphene. The table lists the name by which the peak is most often referred to in literature, the order of the Raman scattering process and whether it is Raman allowed or requires a defect to be activated, the corresponding phonon branch and the position of the peak in the Raman spectrum in cm^{-1} . The $2D'$ peak (in literature also

dubbed 2G peak and - mistakenly - assigned as second overtone of the G peak) is the second overtone of the D' peak and stems from two LO phonons near Γ (see also blue square in Fig. 3.4(a)). Since the two phonons have opposite momenta, it is Raman allowed and may be observed anywhere on a graphene or graphite flake. It is caused by a double-resonant process and positioned around 3240 cm^{-1} if an excitation wavelength of 532 nm or approximately 2,33 eV is used. The 2D' peak, like all peaks in graphene caused by a double-resonant process, is dispersive, that is, its position is dependent on the excitation wavelength. The reason for this is sketched in Fig. 3.5(a): Different excitation wavelengths link valence- and conduction band resonantly for different wavevectors, requiring a different phonon k -vector for the double-resonant process. Since in each case, the phonon branch is probed at a different value in k -space, the phonon energy and thus the peak position may be different. Fig. 3.5(b) shows this in the cases of the D+D'' peak, which shifts rather slowly with excitation energy, and the 2D peak, which is strongly dispersive.

The D+D'' peak is found at about 2450 cm^{-1} . It stems from a double-resonant scattering process involving a TO and an LO phonon from around the K point and its position is also sensitive to the excitation wavelength. It is Raman-allowed and therefore visible in defect-free graphene. For more details regarding this mode, see [Maf07]. The C mode is a rigid-layer shear mode only found in graphene with two or more layers. It can be used to determine the number of layers in a sample but due to its position close to the Rayleigh-scattered light in the spectrum it is quite challenging to measure [Tan12]. The N mode is another mode employed to determine the number of layers in a sample. It stems from a Stokes-Anti-Stokes combination of an LO phonon and a rigid-layer compression mode of graphite [Her12]. The G, D, 2D and D' peaks will be discussed in detail below.

3.3 Raman scattering in graphene

This section concentrates on the concrete example of phonon generation in graphene and graphite. The focus of this section lies on the G, D, 2D and D' modes in graphene and the influence of number of layers, charge carriers and edge chirality on particular peaks.

3.3.1 Raman modes in graphene

In this section, we will introduce the four Raman modes of graphene most commonly used to characterize samples. All peaks are generated by Stokes processes. The most prominent Raman feature, and one of the two allowed first-order Raman processes in graphene results in the so-called **G peak** at about 1580 cm^{-1}

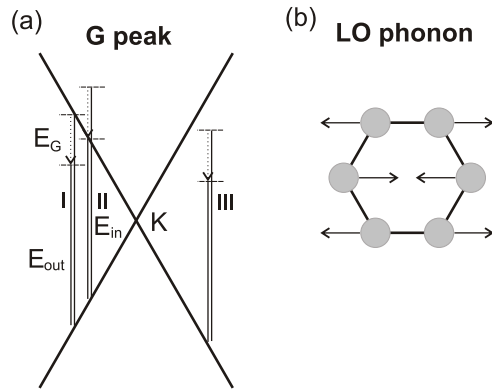


Figure 3.6: (a) three of the scattering processes associated with the G mode. Path (I) and (II) depict incoming and outgoing resonance, path (III) is near-resonant. Scattering processes related to each other as (I) and (II) have in average a phase difference of π if the broadening γ is small and thus their relative contributions to the G peak intensity largely cancel one another. (b) Sketch of the lattice vibration associated with the G peak.

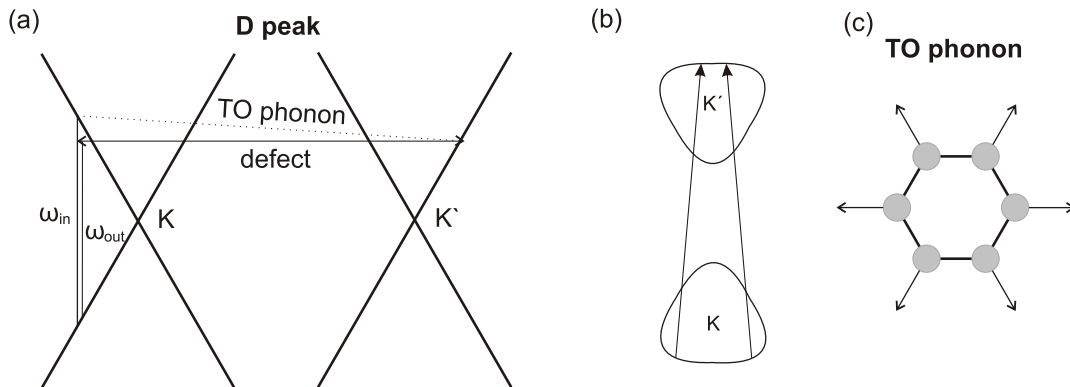


Figure 3.7: (a) one possible double-resonant intervalley scattering process associated with the D mode. The elastic scattering on the defect is necessary for momentum conservation. (b) scattering processes dominating the D peak intensity. (c) Sketch of the lattice vibration associated with the D peak.

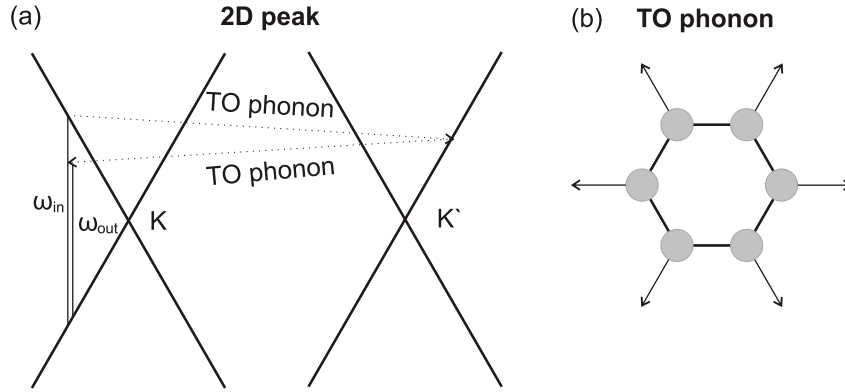


Figure 3.8: (a) double-resonant scattering process involving two TO phonons with opposite momenta resulting in the 2D band. (b) Sketch of the lattice vibration associated with the 2D band.

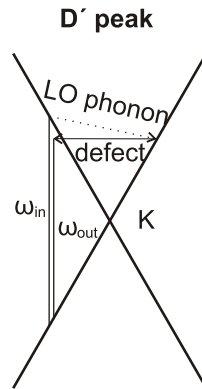


Figure 3.9: double-resonant intravalley scattering process resulting in the D' band.

in electrically neutral single layer graphene (the other being the interlayer shear mode of multilayer graphene [Tan12]). It stems from a single-phonon process involving an optical Γ -point phonon. Fig. 3.6(a) shows three of the scattering processes contributing to the G mode, one with incoming resonance (I), one with outgoing resonance (II) and one near resonance (III). Since Raman scattering is of a quantum mechanical nature and in all scattering processes eventually leading to the G peak the final state is the same, namely, emission of a G mode phonon, all quantum pathways leading to this final state are indistinguishable and may therefore interfere. In the G band, scattering processes related to each other as (I) and (II) have in average a phase difference of π if the broadening parameter γ is small and interfere destructively, strongly diminishing the intensity of the G peak. In this case, the summands in eq. 3.4 for incoming and outgoing resonance have opposite signs and their amplitudes largely cancel each other. If the Fermi

energy is raised (lowered) to near half the energy of the exciting laser light, some of these quantum pathways are blocked and the intensity of the G mode increases. [Bas09] suggests this theoretically and [Che11] gives strong experimental confirmation. Since it is experimentally challenging to shift the Fermi level so far away from the Dirac point, in most samples the G mode intensity is unaltered by a small change in charge carrier density.

Additionally to this effect, the measured intensity of the G peak is governed by the shape and nature of the sample illuminated. In few-layer graphene, it is proportional to the number of layers up to about 20 layers [Gup06], [Gra07]. Casiraghi et al. scanned a laser spot over the edge of a single layer graphene flake and found the intensity of the G peak to be nearly linearly connected to the position of the spot near the edge. When the laser spot was exactly at the edge, half on and half off the graphene flake, the intensity was half of the intensity on the bulk of the flake [Cas09b]. This suggests, that the intensity of the G peak in single layer graphene is linearly connected to the area of graphene illuminated. A representation of the lattice vibration associated with the LO phonon at the Γ -point is sketched in Fig. 3.6(b).

Another Raman feature in graphene is the **D peak**, whose position is sensitive to the excitation wavelength and is found around 1345 cm^{-1} when an excitation wavelength of 532 nm is used. It is caused by a double-resonant second-order Raman scattering process involving one TO phonon from around the K -point and thus is Raman-forbidden, requiring a defect for momentum conservation. Consequently, the D peak is only found at edges or other defect sites and is frequently used to determine the quality of a graphene flake. How the chirality of an edge influences the D peak is discussed below. Fig. 3.7(a) shows one possible double-resonant intervalley scattering process contributing to the D peak. The D mode is dominated by phonons along the $K - M$ line connecting the strongly curved part of the Dirac cone around K with the weakly curved section around K' , see Fig. 3.7(b). Contributions from phonons between Γ and K are weaker due to destructive interference [Nar08]. Contributions from phonons with $q = K$ cancel completely [Nar08]. For more discussion of the issue, see also [Kür02], [Mau04a] and [Fer06]. Fig. 3.7(c) shows a sketch of the lattice vibration associated with the TO phonon at the K point.

The second overtone of the D peak at about 2700 cm^{-1} , called **2D peak**, is depicted in Fig.3.8(a). It is, like the D peak, caused by a double-resonant intervalley scattering process and its position is sensitive to the excitation wavelength. Since here two TO phonons with opposite momenta are involved, the fundamental Raman selection rule is always fulfilled and the 2D peak is allowed everywhere on graphene. In single layer graphene, the 2D peak appears as a single, sharp Lorentzian. In bi- and multilayer graphene, it changes shape and position, allowing for certain distinction of single- and bilayer graphene. This will be discussed below. Fig. 3.11(b) shows a sketch of the lattice vibration associated with the TO phonon at the K point.

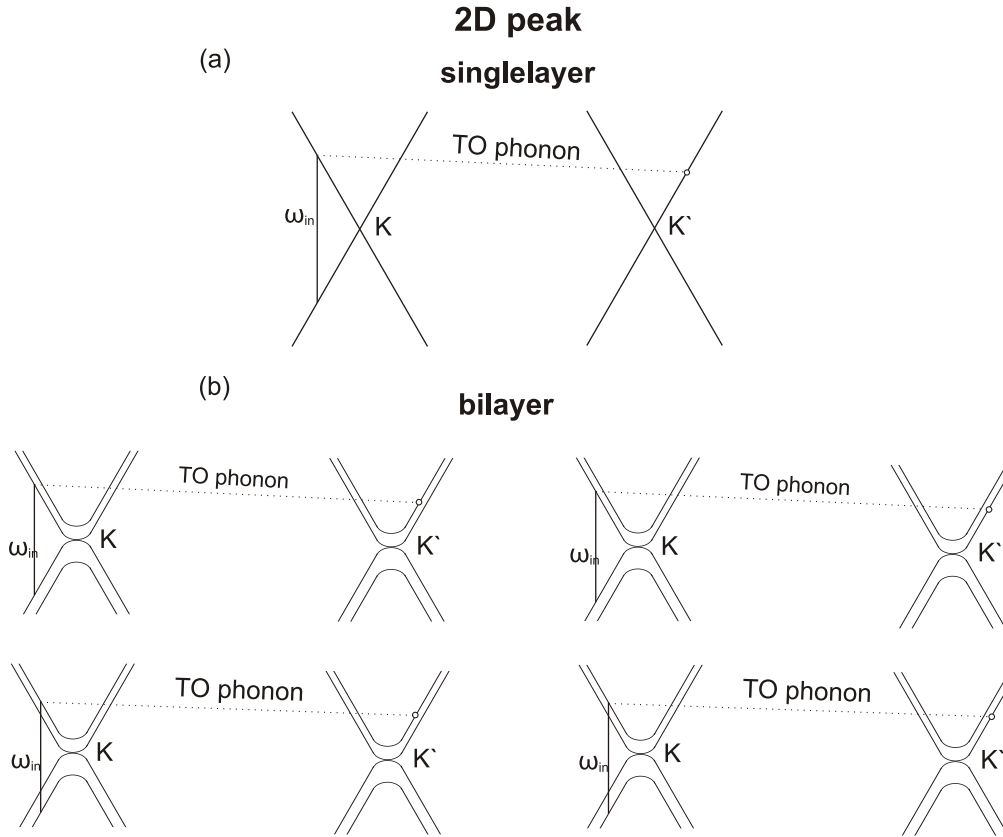


Figure 3.10: double-resonant scattering process resulting in the 2D peak in (a) single layer and (b) bilayer graphene. For clarity, only one phonon is sketched. The open circles denote points of resonance in the K' valley. In single layer graphene, the 2D peak is dominated by one scattering process, resulting in a single, sharp Lorentzian. In bilayer graphene, four scattering processes dominate the 2D peak, resulting in four peaks which comprise the 2D peak in bilayer graphene and give it its characteristic shape.

Fig. 3.9 illustrates a double-resonant intra-valley scattering process involving a defect and an LO phonon, which results in the **D' peak** at 1620 cm^{-1} . Unlike the D peak, this mode does not depend on edge chirality.

For a review of all Raman modes in graphene and graphite, see e.g. [Fer13], [Mal09] and [Rei04], for more information on double-resonant scattering in graphene see, e.g., [Tho00], [Bas08] and [Ven11].

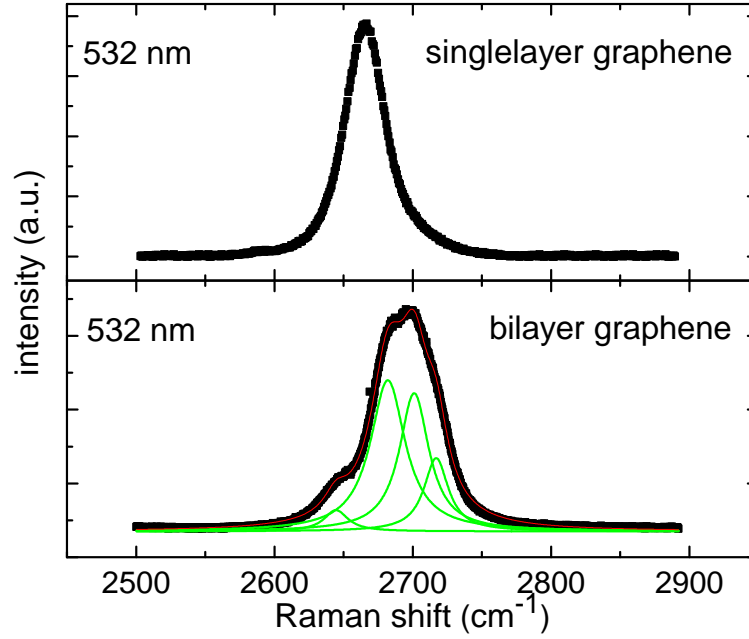


Figure 3.11: 2D peak of mechanically cleaved single layer (top) and bilayer (bottom) graphene. Excitation wavelength 532 nm. In single layer graphene, the 2D peak appears as a single Lorentzian at 2667 cm^{-1} , in bilayer graphene, it consists of four Lorentz peaks and is stiffened with respect to its position in single layer graphene.

3.3.2 Influence of the number of layers on the 2D mode

The 2D peak is caused by a double-resonant intervalley scattering process, as discussed above. This makes it especially sensitive to the shape of the electron dispersion. When comparing single layer and bilayer graphene, the electronic bands are strikingly different. The π and π^* valence- and conduction bands split from one band in single layer to two bands each in bilayer graphene and they are no longer linear close to the Dirac point. This causes the 2D peak scattering process to split from one dominant process to four processes, as indicated in Fig. 3.10. In principle, the incoming light has four possibilities to couple the four bands resulting in eight scattering processes, but according to density functional theory (DFT), the indicated transitions between either the inner or the outer valence and conduction band around the same K point are much stronger than the other two connecting an inner and an outer band around the same K point [Fer06]. After the initial, resonant excitation of an electron-hole pair, the electron is scattered resonantly via a TO phonon to either the inner or the outer conduction band around the K' point. This leads to four slightly stiffened peaks comprising the 2D peak in bilayer graphene resulting in the characteristic peak shape shown in Fig. 3.11. A triple-resonant process, where both the electron and the hole are

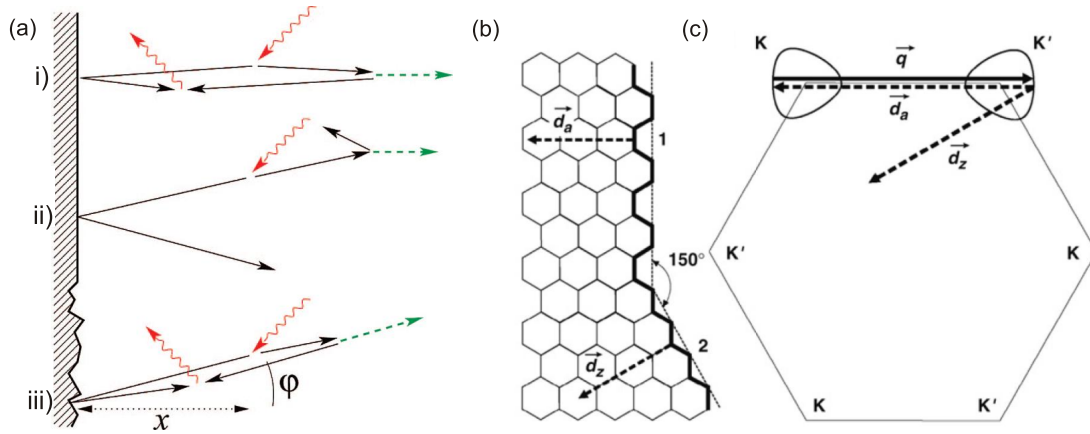


Figure 3.12: (a) Possible scattering mechanisms at the edge of a graphene flake in real space. The wavelike red arrows indicate photons, the solid black lines trajectories of electron and hole, the dashed green line a phonon. i) At an atomically smooth edge, only backscattering of the electron and hole after normal incidence leads to radiative recombination of electron and hole. ii) Oblique incidence scatters electron and hole to different regions of the flake, no radiative recombination. iii) A disordered edge allows backscattering under oblique incidence to end in radiative recombination. Image from [Cas09b]. (b) Real space representation of a graphene flake with an armchair (upper) and zigzag (lower) edge. \vec{d}_a and \vec{d}_z indicate the wavevectors associated with armchair and zigzag edge, respectively. (c) Reciprocal space representation aligned compatibly to the real space in (b). The solid black arrow represents scattering via a TO phonon near the K point, the dashed arrows marked \vec{d}_a and \vec{d}_z denote the \vec{k} -vector provided by an armchair or zigzag edge, respectively. Images (b) and (c) from [Pim07].

resonantly scattered into the valley around K', is also possible, but not sketched here. The 2D peak is dispersive and thus its shape changes for different excitation wavelengths.

3.3.3 Influence of edge chirality on the D mode

As mentioned above, here we will discuss the scattering mechanism giving rise to the D peak in more detail. The D band generally requires a defect to be activated, but the nature of this defect is also crucial to a successful Raman process. That is to say, not every defect contributes to the D peak, for example, armchair edges have a D peak, but zigzag edges do not. **The D peak is forbidden at pure zigzag edges.** Here, we will discuss why only armchair or disordered edges yield a defect suitable to activate the Raman D band and pure zigzag edges do not.

The double-resonant scattering process resulting in the D peak (compare also Fig. 3.7(a)) begins with a resonantly laserexcited electron-hole-pair around the K point. Then the electron (or hole) is scattered by a TO phonon to a state on the Dirac cone around the K' point and scattered back to a virtual state near the original valley via a defect, where it recombines radiatively with its residual hole (or electron). Steps two (scattering by phonon) and three (scattering by defect) may also be reversed in order. A triple-resonant process, where the electron (hole) is scattered by a TO phonon and the hole (electron) is scattered by a defect to the K' valley where they recombine is also possible.

Considering a process which is not fully resonant, one intermediate step violates the energy conservation (eq.3.1) by the amount of the phonon energy $\hbar\omega_D \approx 170$ meV. Hence the lifetime of the electron-hole pair and likewise the duration of the whole scattering process is limited by the uncertainty principle (eq. 3.6) to about $1/\omega_D \approx 3$ fs. This time limit, together with the electron (hole) velocity $v \approx 1.1 \times 10^6$ m/s ≈ 7.3 eV $\text{\AA}/\hbar$ (which is also the slope of the Dirac cones) gives a spatial extension of the process of $v/\omega_D \approx 4$ nm.

Neglecting trigonal warping and assuming that valence and conduction band are perfectly symmetrical, the electron (hole) energy, measured from the Dirac point, is about $\epsilon \approx \hbar\omega_L/2$ where $\hbar\omega_L$ is the laser energy. Neglecting the photon momentum, the k-vector of the electron (hole), measured from the K point, is $k = \epsilon/(\hbar v)$. Then the electron (hole) can be seen as a wave packet of size $\approx 1/k = \hbar v/\epsilon \approx 0.6$ nm.

Electron and hole are created in a region δl with $\hbar v/\epsilon < \delta l < v/\omega_D$. Considering the uncertainty principle (eq. 3.6), momentum conservation holds up to $\delta q \approx \hbar/\delta l < \epsilon/v$. Electron and hole must therefore have approximately opposite momenta after creation, since the photon momentum is negligible. These considerations are also true for phonon emission and radiative recombination. This means that electron and hole have to meet in an area of size δl with approximately opposite momenta in order to recombine radiatively and successfully complete the Raman process.

Therefore, two constraints are imposed on the double-resonant scattering process, namely, (1) the wavevector of the phonon \vec{q} must connect the valleys around K and K' to scatter resonantly and (2) at the end of the process, electron and hole must be in close vicinity to each other. Because photon momentum is very small, the electron (or hole), backscattered by the edge, must meet the edge at normal incidence in order to meet its counterpart, which is backscattered by a phonon, as illustrated in Fig. 3.12(a)i). Since momentum is conserved in an ordered edge, oblique incidence (see Fig. 3.12(a)ii) does not lead to a successful completion of the Raman process. This is only the case in disordered edges, where momentum is not conserved along the edge (Fig. 3.12(a)iii).

Fig. 3.12(b) shows the momenta \vec{d}_a, \vec{d}_z given by an armchair or zigzag edge, respectively. A possible scattering process associated with the D peak is illustrated

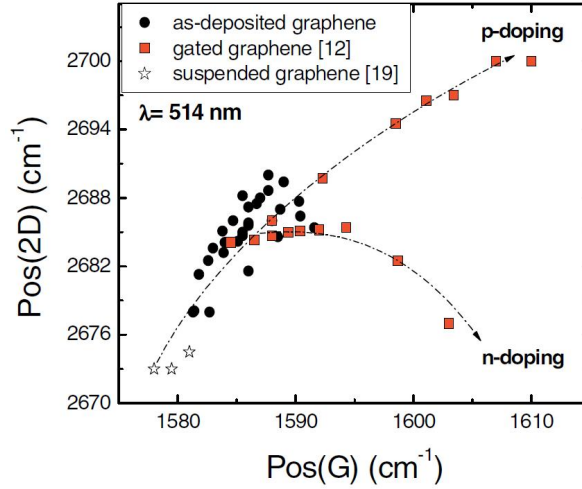


Figure 3.13: Position of the G mode versus position of the 2D mode. Data points marked by orange squares were taken on a gated single layer graphene sample. The correlation is nearly linear for p-type doping and strongly curved for n-type doping. Graph taken from [Cas09a].

in Fig. 3.12(c). A TO phonon with wavevector \vec{q} scatters the excited electron (hole) from a real state in the K valley to a real state in the K' valley. From there it can only be backscattered into its original valley via \vec{d}_a , the momentum given by an armchair edge. The momentum \vec{d}_z given by a zigzag edge scatters the electron (hole) not along the $K - K'$ direction in the crystal but along the $K' - K'$ direction. In this scenario, the overall momentum in the scattering process is not conserved and zigzag edges do therefore not contribute to the Raman D band. This does not touch the D' peak. This peak is generated by an intra-valley scattering process, which can be successfully completed at both armchair and zigzag edges.

For experiments on this issue, see also [Can04], [Cas09b] and [Kra10].

3.3.4 Influence of charge carriers on the G and 2D modes

The G peak is especially sensitive to a change in the charge carrier density in graphene and reacts quite strongly already to a small number of charges. Thereby it exhibits the same behavior for electron- as for hole-doping.

For electrically neutral graphene, the Fermi level E_F is at the Dirac point and the Kohn anomaly, which appears at $2k_F$ [Koh59], in the doubly-degenerate optical phonon is exactly at the Γ -point since $k_F = 0$. The Kohn anomaly is a softening of the phonon due to electron-phonon interaction. When E_F is raised (lowered), the Fermi surface changes from a point to a circle and the value of the Fermi

wavevector \vec{k}_F increases from zero to a non-zero value. As the Kohn anomaly is coupled to \vec{k}_F , it, too, moves away from $k = 0$ ([Koh59]) and the phonon stiffens at the Γ -point. Consequently, the G peak, which probes the phonon dispersion at the Γ -point, stiffens as the graphene changes from electrically neutral to doped. According to [Yan07], [Pis07], [Das08] and the measurements presented in chapter 5.2, the G mode shifts by 1 cm^{-1} for every $4.5 \times 10^{11} \text{ cm}^{-2}$ charge carriers, starting at 1580 cm^{-1} for electrically neutral graphene.

While $|E_F| < \hbar\omega_G/2$ where ω_G is the angular frequency of the G mode, the G peak is Landau-damped [Yan07]. In this case, the G mode phonons can decay into electron-hole pairs. These are real transitions that conserve energy and momentum. Since G peak phonons have only small momentum, these must be almost vertical transitions with very small wave vector transfer. To satisfy the Pauli principle, such decay processes are only allowed if $|E_F| < \hbar\omega_G/2 \approx 100 \text{ meV}$ [Yan07]. This threshold corresponds to a charge carrier density of $1.1 \times 10^{12} \text{ cm}^{-2}$. In the Landau-damping regime, full width at half maximum (FWHM) of the G band is about 13 cm^{-1} , outside it, FWHM is about 9 cm^{-1} . Theoretically, the change in FWHM should be sudden, but in experiments it is observed as a gradual shift. This is presumably due to charged impurities trapped in the substrate or arbitrary, localized charges on the flake caused by self-doping [Per06], and chemical adsorption. Such disorder gives rise to electron-hole puddles in electrically neutral graphene, and allows the presence of local charge carriers even though the average charge carrier density vanishes [Mar08].

Although the TO phonon also exhibits a Kohn anomaly at the K point, the 2D peak associated with this phonon does not react as sensitively to small changes in charge carrier density as the G mode. However, when large amounts of electrons (holes) are introduced, it, too, begins to shift position, but asymmetrically for electron- and hole-doping, unlike the G mode.

For electron concentrations up to about $3 \times 10^{13} \text{ cm}^{-2}$, the position of the 2D mode remains nearly stagnant (shift $< 1 \text{ cm}^{-1}$, see [Das08]), then it softens. For hole-doping, the 2D band is unmoved until $5 \times 10^{12} \text{ cm}^{-2}$, then it stiffens. A change in FWHM has not been observed in the literature.

This sensitivity of the position of both the G and the 2D mode to charge carriers and their different reactions toward electrons and holes make these Raman modes an ideal tool to identify amount and nature of doping in a flake. Plotting the position of the 2D band $\text{Pos}(2D)$ via the position of the G band $\text{Pos}(G)$ gives a characteristic shape and enables one to easily distinguish between electron- and hole-doping. The orange squares in Fig. 3.13 depict data points gathered on a gated flake, representing the change in position for n-type and p-type doping, respectively. If the flake is p-type doped, G peak and 2D peak move with almost constant shift, creating a nearly straight branch in the plot. For electron doping, the irregular behavior of the 2D peak leads to a downwards-bent branch for n-type doping.

For theoretical discussions of this topic, see [Pis04], [Laz06], [Net07] and [Bor10], for experiments, see [Yan07], [Pis07] and [Das08].

Chapter 4

Sample fabrication and experimental setup

This chapter introduces the samples discussed in this work and the preparation processes for both circular and hexagonal antidots. Finally, it describes the two measurement setups used in this work.

4.1 Sample fabrication and samples

In this work, one single layer flake with a backgate and two types of nanopatterned graphene flakes were studied: graphene with circular antidots and graphene with hexagonal antidots.

4.1.1 General preparation of single layer graphene and substrate

All samples were prepared from natural graphite by the well-known mechanical cleavage method (e.g. [Nov05]) on heavily p-doped Si, capped by 300 nm SiO₂, to allow backgating. The substrate is also tailored to allow easy identification of graphene flakes in an optical microscope using white light. Graphene has a universal value of light absorption, $\pi\alpha = 2.3\%$, where α is the fine structure constant[Nai08]. Other two-dimensional semiconductors, like InAs nanomembranes, have been found to have a step-like absorption. As the excitation energy is tuned, the absorptance increases in steps whose height is independent of the material thickness in the sample[Fan13]. The combination of graphene's significant absorption and the interference aided by the transparent oxide layer of the

substrate, allows the detection of even single layer flakes[Bla07]. However, if the thickness of the oxide layer is changed by only 5% to 315 nm, the contrast is significantly lowered[Bla07]. Therefore, detection depends on the thickness of the oxide layer and the color of the illumination.

A similar effect is observed in the Raman modes of graphene on Si/SiO₂ wafers. Multiple Raman scattering events at the interfaces allows interference to alter the observed intensity of the Raman modes[Yoo09], making it dependent on both oxide layer thickness and the wavelength of the observed Raman light, which in turn depends on the excitation wavelength. This has only an impact on the interpretation of measurements, if the absolute intensity of a peak is considered or if intensities of different peaks or one peak measured with different excitation wavelengths are compared. If one compares only intensities of one mode, measured with the same excitation wavelength, this has no implications.

All substrates are patterned with a gold alignment grid to allow easy access to pre-identified flakes. With the exception of the gated flake, all samples were fabricated without contacts to avoid unintentional doping by vacuum deposited metal.

4.1.2 Single layer graphene with backgate

One otherwise unaltered single layer graphene flake was contacted and gated to allow tuning of the charge carrier density in the flake. The sample was prepared by Dr. Jonathan Eroms.

From transport experiments on similar samples, the applied backgate voltage (V) V_{gate} in this sample can be linked to the number of electrons n in the flake as $n = 7.2 \times 10^{10} \text{ cm}^{-2} \times (V_{gate} - V_{Dirac})$ with V_{Dirac} the backgate voltage (V) necessary to shift the Fermi level to the charge-neutrality point.

The Fermi energy in graphene changes as $E_F(n) = \hbar |v_F| \sqrt{\pi n}$ with $v_F = 1.1 \times 10^6 \text{ m/s}$ the Fermi velocity.

4.1.3 Single layer graphene with circular antidots

Four different graphene flakes, each including a single layer part, were patterned with periodic arrays of circular holes, so-called circular antidots. The nanopattern was written on Polymethylmethacrylate (PMMA) resist using electron-beam lithography (EBL), after developing the resist, the antidots were etched by reactive ion etching (RIE) with oxygen as reactive gas. We prepared square antidot lattices with four different lattice constants ranging from 80 nm to 400 nm and two types of hole diameter, 50 nm and 60 nm. The samples are named **circAD** to indicate circular antidots, followed by the **lattice constant** in nm. If a distinction between larger and smaller hole diameters is necessary, the lattices with smaller antidots are denoted (**s**). If possible, the flakes were left partially unpatterned to

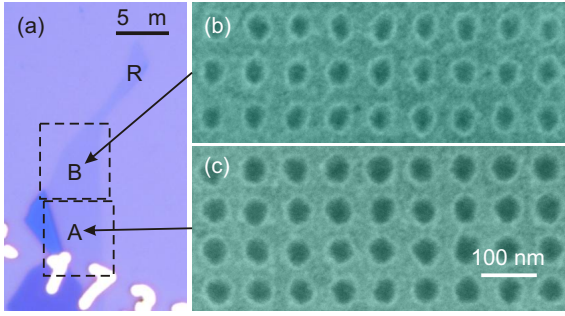


Figure 4.1: (a) microscope image of sample *circAD80*. The dashed black rectangles indicate, where the flake has been patterned with circular antidot lattices. (b), (c) scanning electron microscope images of areas B and A, respectively. Antidots in A have a slightly larger diameter (60 nm) than in B (50 nm).

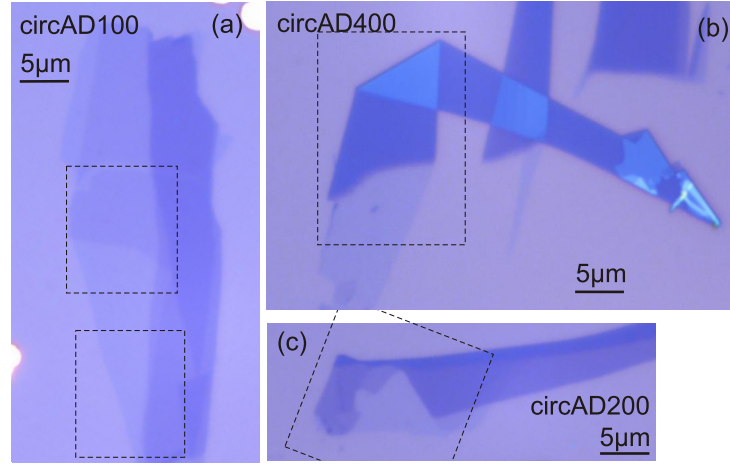


Figure 4.2: microscope images of sample (a) *circAD100*, (b) *circAD400*, and (c) *circAD200*. Black dashed rectangles mark which areas were etched with antidot lattices. (a) sample *circAD100* has single- and bilayer, both with antidots and without as reference section. (b) sample *circAD400* has a single layer area with antidots and an unpatterned reference area. (c) sample *circAD200* has a small single layer area with antidots, but no single layer reference section.

provide a reference section on each sample.

All samples of this series are courtesy of Dr. Jonathan Eroms.

To evaluate the Raman data gathered on all EBL and RIE treated samples, it is necessary to take the influence of EBL and RIE on Raman spectra in graphene into account. Reference [Fan11] finds, that spin-coating PMMA resist onto graphene results in a small amount of disorder in the flake, which is reflected in the Raman spectrum in a D peak and a decrease in the G peak intensity. However, this disorder, which is presumably caused by adsorbates, was found to resist an acetone bath but may be removed by annealing [Fan11]. Since the samples with circular antidots are not heated in the patterning process, there may be residual adsorbates on the surface. The samples with hexagonal antidots (see below), however, are annealed in the etching process and should therefore not carry adsorbates caused by PMMA coating.

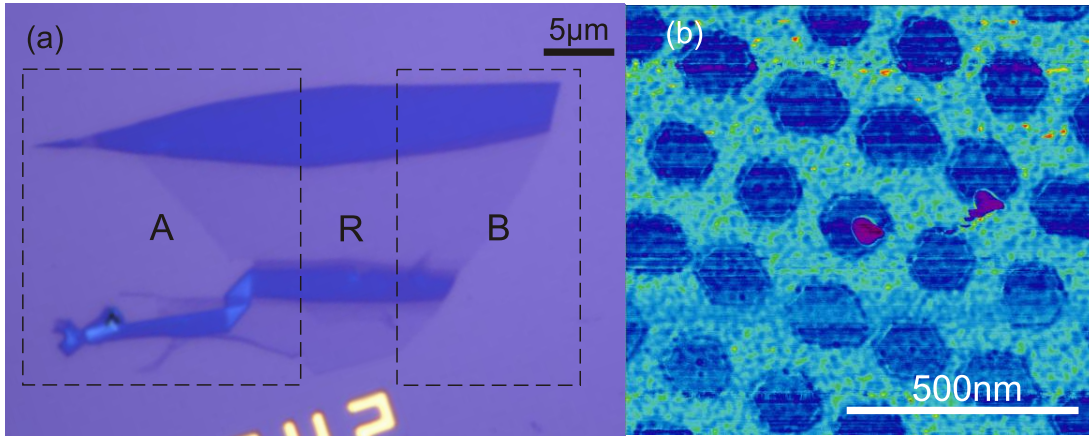


Figure 4.3: (a) microscope image of sample *hexAD(200/400)*. The dashed black rectangles mark where the flake has been patterned with antidot lattices. Area A has a lattice constant of 400 nm, area B of 200 nm. Region R was left unpatterned as reference section. (b) phase contrast AFM image of the antidot lattice in area B after the second anisotropic etching step. Note the hexagonal shape of many antidots.

Sample **circAD80** is a single layer graphene flake patterned with two lattices of circular antidots with 80 nm lattice constant, one lattice with 50 nm hole diameter, the other lattice with 60 nm hole diameter, and a reference section. Fig. 4.1 shows a microscope image and two scanning electron microscope (SEM) images of *circAD80*. The black rectangles mark where the flake was patterned. The antidots in area A have a slightly larger diameter (60 nm) than in B (50 nm).

Sample **circAD100** consists of a single layer and a bilayer part. It was patterned with two antidot lattices with 100 nm lattice constant, one with 50 nm and one with 60 nm hole diameter. Both, in the single- and the bilayer region, a reference section was left unpatterned. For a microscope image of the flake with sketched antidot lattices, see Fig. 4.2(a). This flake will be introduced again in more detail in chapter 5.

Sample **circAD200** has a small single layer area etched with antidots with 200 nm lattice constant and 60 nm hole diameter, but no single layer reference section. Fig. 4.2(c) shows an image of the flake.

Sample **circAD400** has a large single layer region patterned with an antidot lattice with 400 nm lattice constant and 60 nm hole diameter. Part of the single layer was left unpatterned, as may be seen from Fig. 4.2(b).

4.1.4 Single layer graphene with hexagonal antidots

With care, it is possible to selectively etch carbon atoms located at specific edge sites. This bears the possibility to create devices where one type of edge chirality greatly prevails. In the literature, two approaches to anisotropic etching can be found: One through catalysts, where metallic or non-metallic nanoparticles move along a graphene flake and etch trenches [Dat08], [Cam09], [Gao09], the other where pristine or prepatterned flakes are subjected to heating in different atmospheres [NI10], [Yan10], [Shi11]. The advantage of the non-catalyzed form over the catalyzed one is that pre patterning of the flakes allows position control over the edges and e.g. enables one to leave an unpatterned reference section, whereas the movements of the catalyst nanoparticles over the flake are, due to the distribution process of the nanoparticles, uniform and largely random. Only the angles between trenches favor 60° and 30° , as a result of the graphene lattice. Since reference sections were wanted, a non-catalyzed etching process was chosen for the sample presented in this work.

The sample was processed by Florian Oberhuber.

A graphene flake with a very large single layer part was prepared with two hexagonal antidot lattices and a reference section. First, the flake was patterned with circular antidots with **EBL and RIE**, as described above. Diameter of the circular antidots was 40 nm in both lattices. Then followed a **preparation step** in which the flake was heated in a quartz tube reactor with a stainless steel grid to change the chemical environment of the flake for the ensuing anisotropic etching step. The sample was then etched without the grid in the reactor at a temperature $T \approx 820^\circ\text{C}$ in a flow of Ar gas (purity $\geq 99.9999\%$, $\text{O}_2 \leq 0.5$ ppm) at ambient pressure. During this etching step, the circular antidots grow to hexagonal antidots, because not all atoms along the edge of each antidot are removed equally. The aim is to predominantly etch atoms at armchair sites and consequently be left with antidots which have predominantly zigzag edges, creating the honeycomb outline of the antidots. This **anisotropic etching** step was then repeated once more. After the first anisotropic etching step, antidot diameters were between 70 nm and 80 nm, after the second etching step, between 125 nm and 145 nm.

It is still speculative, how exactly the anisotropic etching comes to pass and why the preparation step is necessary for anisotropic etching in single layer graphene, but not in bi- or multilayer graphene [Obe13]. The best performance for anisotropic etching was found in a narrow temperature range around $T 820^\circ\text{C}$, with lateral etch rates $\approx 20\text{nm/h}$ for single layer graphene [Obe13]. Reference [NI10] suggests that the etching reaction occurs between graphene and oxygen atoms from the SiO_2 -layer, however, Oberhuber et al. observed anisotropic etching in the top layers of multilayer graphene with intact bottom layers, insulating the etching site from the SiO_2 [Obe13]. They suggest that the reaction involves gaseous O_2 with concentrations ≤ 0.5 ppm in the Ar atmosphere, as an additional flow of H_2 gas could inhibit the etch reaction [Obe13]. See especially the supplementary

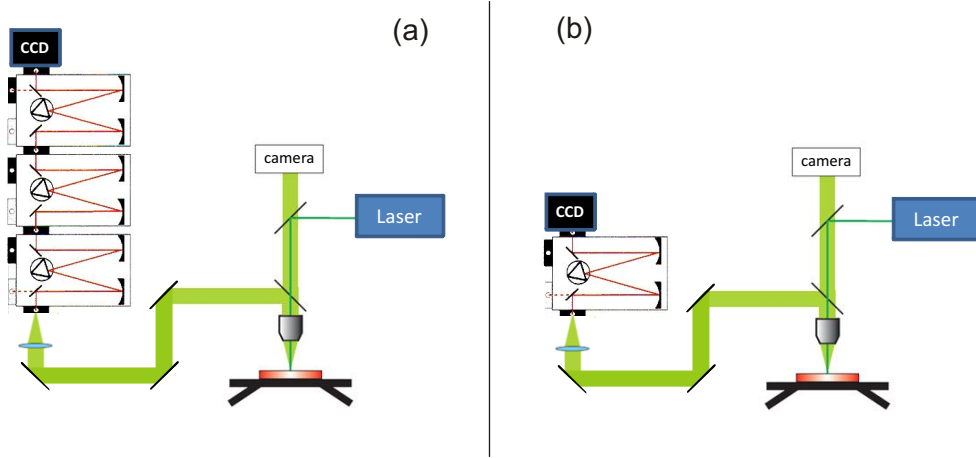


Figure 4.4: (a) *Micro-Raman setup used to record spectra on the series of samples with circular antidots. Excitation source was a 532 nm diode-pumped solid state laser. Samples were mounted on an x-y-stage with 100 nm minimal step size and spectra were recorded using a triple Raman spectrometer equipped with a liquid nitrogen-cooled CCD detector.* (b) *Micro-Raman setup used to monitor the evolution hexAD(200/400). Excitation source was a circularly polarized 532 nm diode-pumped solid state laser. Spectra were recorded using a single stage Raman spectrometer equipped with 1200 grooves per mm holographic grating and a thermoelectrically cooled CCD detector.*

material to [Obe13] for details on this discussion.

Fig. 4.3(a) shows a microscope image of the sample. The dashed black rectangles indicate the etched areas of the flake. The lattice constant in area A is 400 nm and 200 nm in area B. Area R was left unpatterned as reference section. Fig. 4.3(b) shows an AFM image of part of area B with 200 nm lattice constant. The AFM image was acquired after the last Raman scan.

In this particular flake, its evolution was carefully monitored by Raman spectroscopy, meaning that after each preparation step two scans of the flake were made. One scan monitored the D and G bands, the other the 2D band. No scanning electron microscopy (SEM) images were taken until after the final Raman scan was completed to not contaminate the flake with charge carriers or impurities.

This sample will be referred to as **hexAD(400/200)**, since it has two antidot lattices with 400 nm and 200 nm lattice constant, respectively.

4.2 Experimental setup

This section introduces the two setups used to acquire, both, Raman scans and individual Raman spectra presented in this thesis.

All Raman spectra shown in this work were recorded in backscattering geometry at room temperature under ambient conditions.

On the gated single layer graphene and on the first series of samples with circular antidots, experiments were performed using a linearly polarized 532 nm diode-pumped solid state laser with 50 mW power and an 100x objective lens, as sketched in Fig. 4.4(a). Samples were mounted on an x-y-stage with 100 nm minimal step size. Spectra were recorded using a triple Raman setup equipped with 1500 grooves per mm grating and a liquid nitrogen-cooled CCD detector. Stages one and two of the triple spectrometer act as adjustable bandpass, used to suppress the elastically scattered light, and allowing detection of modes with very small Raman shifts ($\approx 20 \text{ cm}^{-1}$).

The spatial resolution of this setup is about 800 nm. The setup allows both scanning Raman spectroscopy and the collection of single spectra. Spectra gathered in a scan were evaluated automatically for peak height, width, and position, by software written in LabView. These matrices were then processed in Origin to create false-color plots.

The Raman scans are made up of spectra recorded for 20 s each. For spectra gathered individually, outside a scan, exposure times were up to 180 s.

All Raman scans monitoring the evolution of the sample hexAD(400/200) were performed using a circularly polarized 532 nm diode-pumped solid state laser with 50 mW power and an 100x objective lens. See Fig. 4.4(b) for a schematic. The sample was mounted on an x-y-stage with 100 nm minimal step size. Spectra were recorded using a single stage Raman spectrometer equipped with 1200 grooves per mm holographic grating and a thermoelectrically cooled CCD detector. A long-pass filter was used to suppress the Rayleigh scattered light.

Raman scans were evaluated automatically by software written in LabView for peak height, width, and position. False-color images were created in Origin.

The spatial resolution of this setup is about $1 \mu\text{m}$. Since this setup has fewer losses than the one described above, recording times ranging from 0.5 s up to 5 s per spectrum in a scan were sufficient.

Chapter 5

Experimental results

This chapter begins with an introduction to typical Raman spectra of single-, bi- and multilayer graphene. We present how false color images are constructed from Raman scans and illustrate the dispersive behavior of some modes. Then, we will introduce Raman spectra recorded on single layer graphene with charge carrier density varied by a backgate, with focus on the G mode. Next, we will cover Raman scans and single spectra recorded on single layer graphene samples etched with circular antidots. Lastly, we will use micro-Raman scans to monitor the successive steps of treatment necessary to anisotropically etch a flake with hexagonal antidots using the example of a large single layer flake.

5.1 Basic information to scanning Raman spectroscopy in graphene

This section introduces some of the most prominent Raman modes in graphene (D, G, D+D'', and 2D) again and uses certain peaks to illustrate basic properties of graphene, like the difference between the electronic bands in single layer and bilayer graphene as it is reflected in shape and position of the 2D peak, and the dispersive behavior of peaks stemming from double-resonant processes using the 2D and the D+D'' peak as an example. We will begin by illustrating the creation of false-color plots from Raman scans.

Fig. 5.1 (a) shows a microscope image of a single layer graphene flake. The flake consists of three separate islands, a topmost, vaguely triangular one, a middle part shaped like a hatchet and a thin strip on the bottom. In the topmost part, one edge is folded upwards and in on itself, creating a thin strip of folded graphene, consisting of more than one layer. Fig. 5.1 (b) shows a false color plot

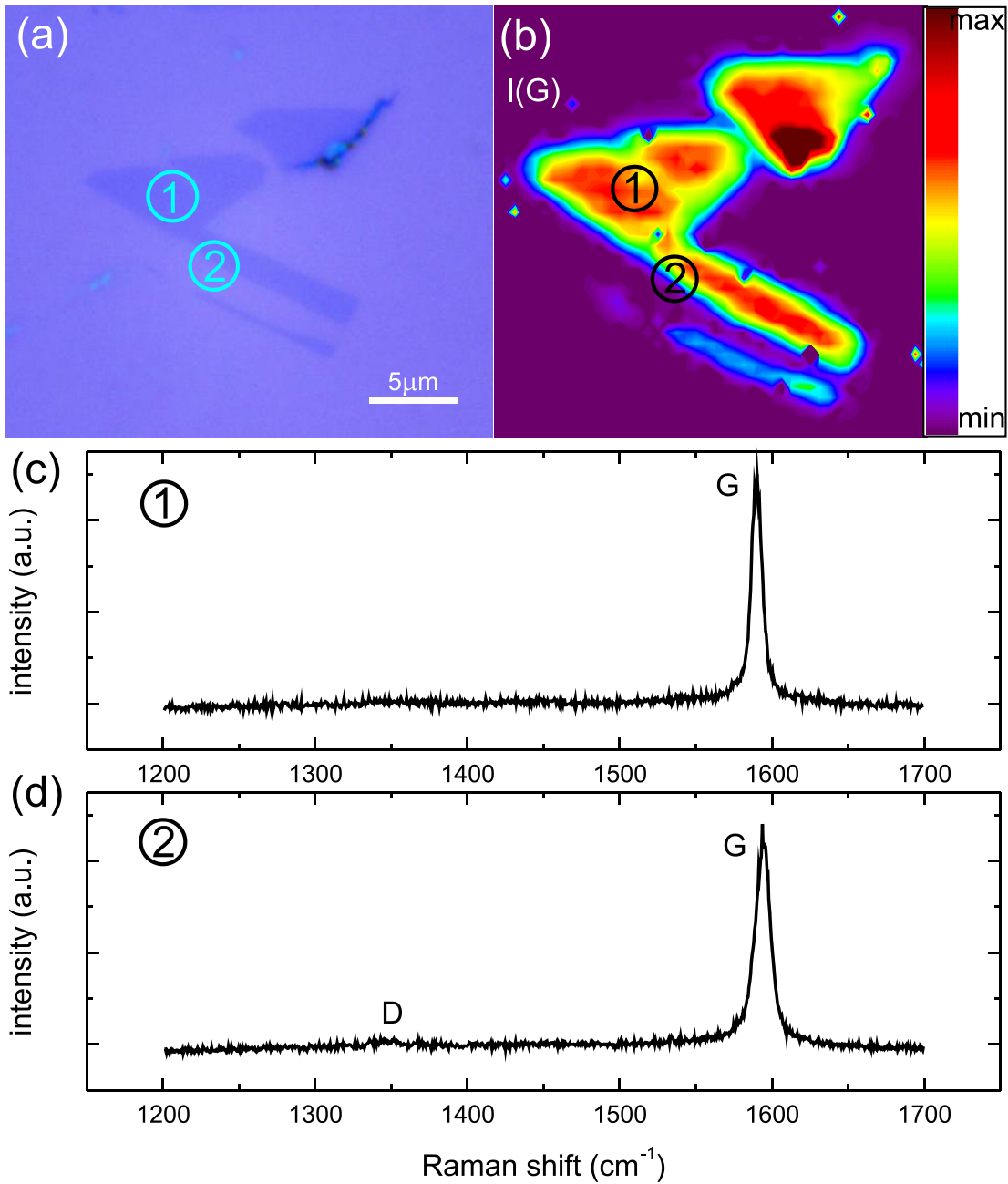


Figure 5.1: (a) optical microscope image of a single layer graphene flake consisting of three parts. Note the folded rim on the right side of the upper part. 1 marks a spot in the middle of the flake, 2 a spot on the edge. (b) false color plot displaying the G mode intensity. Color scale is shown on the right. (c) Spectrum collected with the laser directed at the spot marked 1 in (a). This is a spectrum typical of a pristine, single layer graphene flake. (d) Spectrum with the laser directed at the spot marked 2 in (a). This spectrum was gathered at a flake edge and shows a D peak additionally to the G peak.

of the G mode intensity of this flake. The false color plot is the result of a Raman scan, whereby Raman spectra depicting the D and G modes in a rectangular area around the flake were collected for 20 s every 500 nm.

Fig. 5.1 (c) and (d) show two exemplar spectra, gathered at locations marked 1 and 2 in both the microscope image and the false color plot. To construct the false color plot depicted in (b), in every spectrum, the G peak was fitted with a Lorentzian and the height of the fitted peak of every spectrum was evaluated and plotted into a 2D matrix, which was translated into colors. The color scale used is shown in (b) on the right. The result is a faithful, if slightly blurred image of the flake, with heightened intensity along the folded graphene in the top part. Since the laser spot used for the scan has a diameter of approximately 500 nm, there are spectra where the laser spot is half on and half off the flake, compare location 2, yet the result in the false color plot is not a square half filled with high intensity and half filled with low intensity, but a full square filled with an average intensity. Therefore, from a mathematical viewpoint, the false color image is a convolution of the flake with the intensity profile of the laser spot. This fact explains the slight blurriness of the image and the lowered intensity along the edges in (b). When, while generating a figure in Origin, the option “fill to grid lines” is selected, the individual values are displayed in a square lattice; “fill to contour lines” leads to further smoothing.

The spectrum shown in (d) shows, aside from the G peak, also a very small D peak, since it was collected at an edge of the flake. Since the false color image shown in (b) only depicts the intensity of the G mode, this information is completely lost in the false color image, as is any information about position or linewidth of the G mode, which was of course included in the original spectra. To access this information, one must construct a false color plot for each feature. Therefore, a false color plot graphically illustrates the evolution of one Raman feature (e.g. the intensity of a mode) over an entire flake, but one plot is also limited to one information.

Fig. 5.2 (a) shows a microscope image of a flake consisting of a single layer part on the bottom and a multilayer part on the top. The flake and its two parts are highlighted by a white outline. Fig. 5.2 (b) shows the 2D peak in single layer graphene (top) and bilayer graphene (bottom). Fig. 5.2 (c) and (d) show false color plots depicting the full width at half maximum (FWHM) of the 2D peak and the position of the 2D peak, respectively. Scale bars may be found on the right of each image.

As introduced in chapter 3, the one valence band and one conduction band of single layer graphene split into two bands in bilayer graphene and graphite and this is reflected in the shape and position of the 2D peak, due to the double-resonant nature of its Raman scattering process. In single layer graphene, the 2D peak appears as a single, sharp Lorentzian around 2670 cm^{-1} , if an excitation wavelength of 532 nm is used, with FWHM of about 30 cm^{-1} , see top half of Fig. 5.2 (b). In bilayer graphene and again with 532 nm excitation wavelength, the 2D mode is

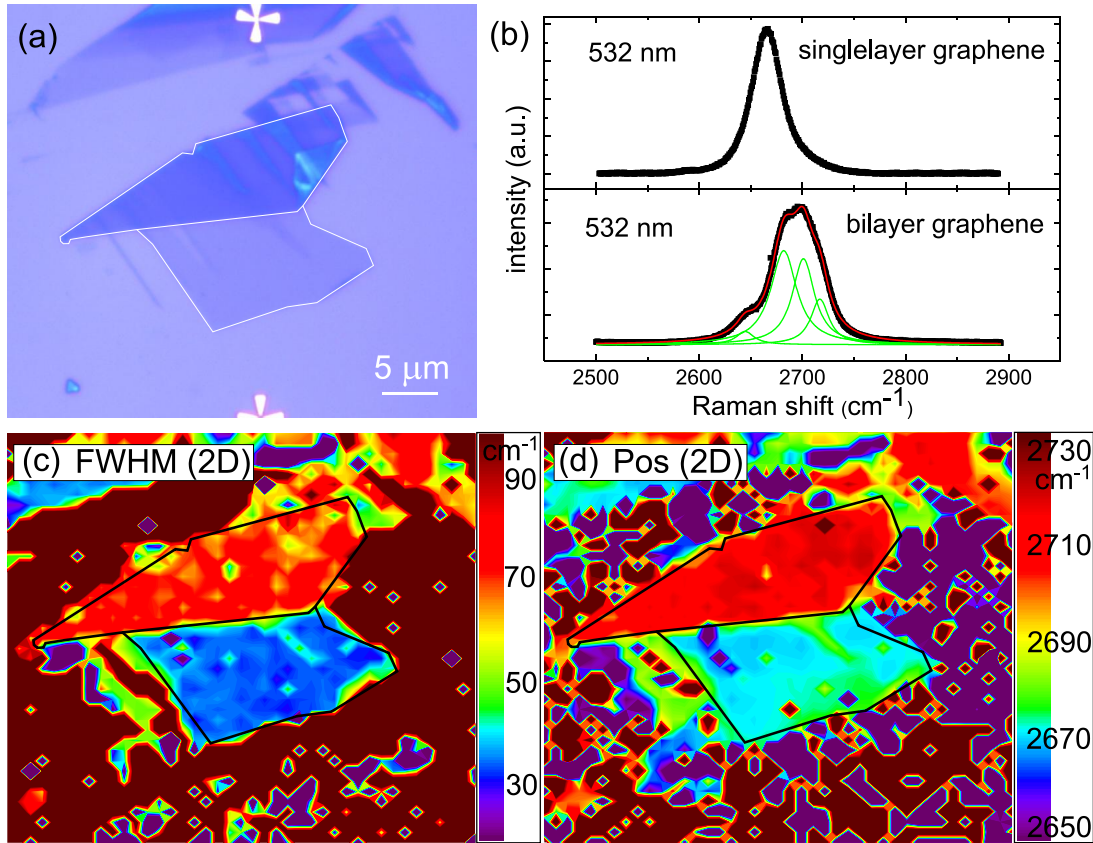


Figure 5.2: (a) optical microscope image of a graphene flake comprising a multi-layer (top) and single layer (bottom) part, outlined in white. (b) Spectra showing the 2D peak in single layer graphene (top) and bilayer graphene (bottom). In bilayer graphene, the 2D peak consists of four individual peaks, reflecting the change in valence- and conduction band, which split from one in each in single layer graphene to two each in bilayer graphene. (c) false color plot displaying the full width at half maximum (FWHM) of the 2D peak linewidth. $FWHM(2D)$ is small on single layer and larger on multilayer graphene. (d) false color plot displaying the position of the 2D peak. It is up-shifted on the multilayer graphene part of the flake with respect to the single layer graphene part.

up-shifted to about 2700 cm^{-1} and broadened to about 70 cm^{-1} FWHM, since it now consists of four Lorentz peaks, as shown in the bottom part of Fig. 5.2 (b) in green.

Fig. 5.2 (c) shows a false color plot of FWHM of the 2D mode, built from a scan of the flake shown in (a). As expected, $\text{FWHM}(2\text{D})$ is about 30 cm^{-1} in the single layer area (bottom) in the multilayer area (top), $\text{FWHM}(2\text{D})$ is broader, about $70\text{ cm}^{-1} \pm 10\text{ cm}^{-1}$. Of course, this second number has a large error, since the 2D peak in spectra taken in the Raman scan is fitted with a single Lorentzian, which is a very good fit for the 2D mode in single layer graphene but not in bi- or multilayer graphene.

Likewise, the position of the 2D mode follows the theory outlined in chapter 3. It is found around 2670 cm^{-1} in the single layer part on the bottom and around 2710 cm^{-1} in the multilayer part on the top.

This paragraph illustrates the dispersiveness of double-resonant Raman modes using the examples of the $\text{D}+\text{D}''$ mode and the 2D mode. Fig. 5.3 (a) shows both modes measured in single layer graphene using 561 nm , 532 nm , and 473 nm as excitation wavelengths. The inset shows the $\text{D}+\text{D}''$ peak in detail. The dashed vertical lines mark the respective peak centers in the spectrum taken with 561 nm excitation wavelength. It is evident from (a) that both peaks shift position when the excitation wavelength is changed. This softening or stiffening, respectively, is explained in the images in Fig. 5.3 (b) and (c). Fig. 5.3 (b) shows a double-resonant scattering process, connecting the valleys around K and K' . The 2D peak and the $\text{D}+\text{D}''$ peak are both caused by such a scattering process involving two TO phonons with opposite momenta in the case of the 2D peak and a TO and an LA phonon with opposite momenta in the case of the $\text{D}+\text{D}''$ peak. If the excitation wavelength is changed, the double-resonance condition selects a TO or LA phonon, respectively, with a different momentum. This means that the phonon dispersion is probed at a different point, and therefore the energy of the selected phonon may of course also differ, see Fig. 5.3 (c). Since the phonon energy directly relates to the position of the Raman peak, the observed mode shifts with excitation energy.

5.2 G peak position and lineshape in single layer graphene with backgate

This section concentrates on the influence of charge carriers on the Raman G mode in a backgated single layer graphene flake under ambient conditions at room temperature. We will find that the G peak stiffens and sharpens, when the Fermi level is moved away from the charge-neutrality point. The stiffening is attributed to the Γ -point Kohn anomaly removing from $k = 0$. The change in lineshape is

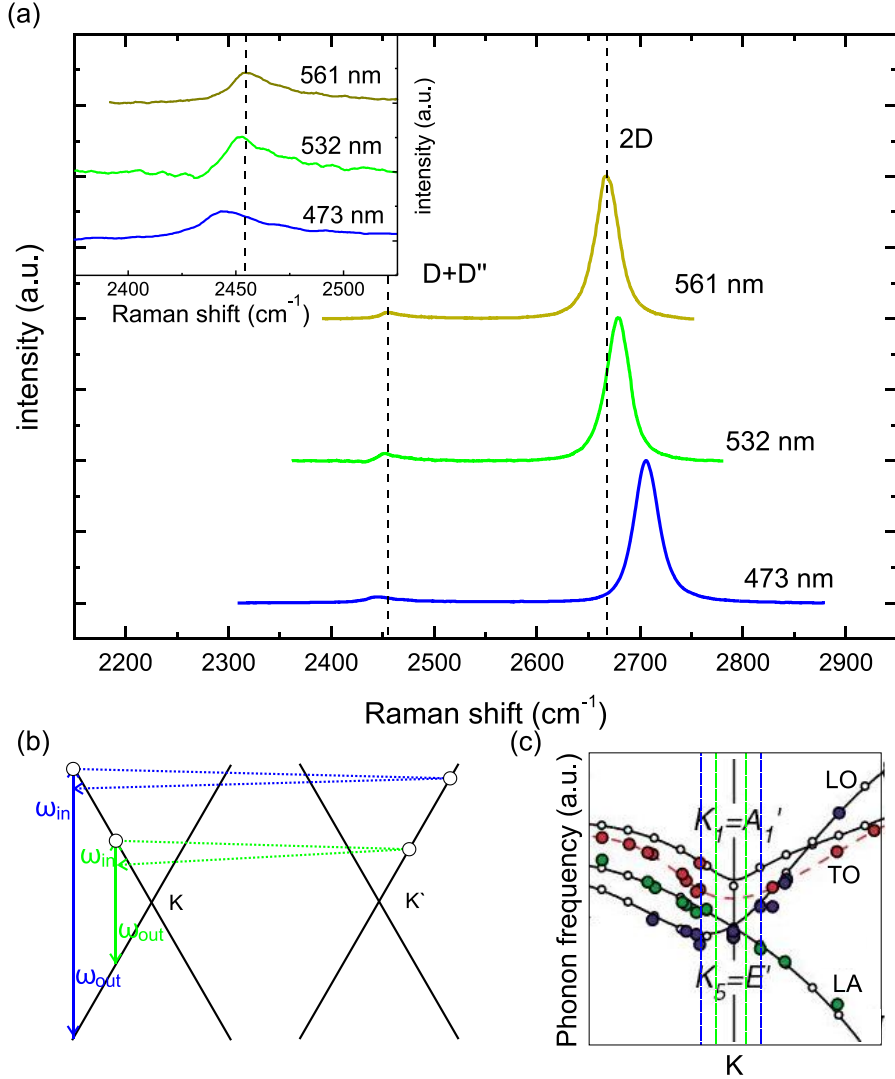


Figure 5.3: (a) Raman spectra concentrating on the $D+D'$ mode and the $2D$ mode in single layer graphene, measured using 473 nm, 532 nm, and 561 nm, respectively, as excitation wavelengths. The dashed vertical lines are a guide to the eye centered on the respective peaks in the 561 nm spectrum. The $D+D'$ mode softens and the $2D$ mode stiffens as the excitation wavelength is changed from yellow to blue. The inset shows a close-up of the $D+D'$ mode. (b) schematic demonstrating the change in double-resonant scattering process as the excitation wavelength is changed. The double-resonance condition selects a different phonon with different \vec{k} -vector and phonon energy in each case. (c) Close-up of the phonon dispersion of graphite around the K point. Image adapted from [Mau04b]. The dashed vertical blue and green lines show qualitatively how the double-resonance condition selecting a phonon with a different \vec{k} -vector influences the energy of the selected phonon and thus the position of the resulting Raman peak.

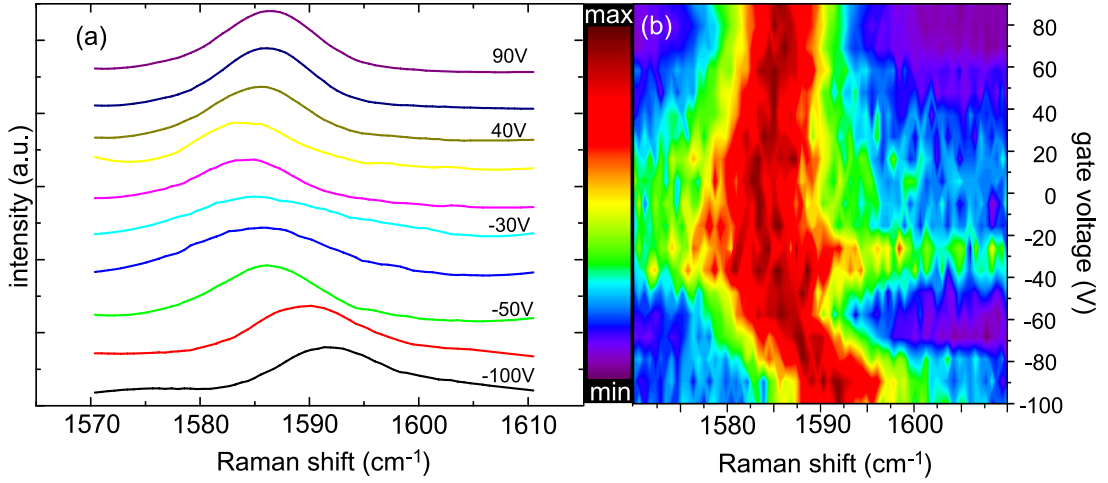


Figure 5.4: (a) Selected spectra taken on single layer graphene with different backgate voltages. The G peak position is lowest at -30 V and stiffens for both higher and lower gate voltages. (b) All spectra of the same measurement cycle combined to a false-color plot. The relation between intensity and color scale is shown on the left. Here, it is striking, that the G peak not only shifts, but also broadens around -30 V.

attributed to Landau-damping, active if E_F is near charge-neutrality and broadening the shape of the G peak significantly. If $E_F > \hbar\omega_G/2 \approx 100$ meV, when ω_G is the frequency of the G peak, the Landau-damping is lifted and the G peak sharpens.

We have contacted a single layer graphene flake, added a backgate (for details, see chapter 3) and observed the behavior of the G peak as the backgate voltage V_{gate} was changed. To avoid sample damage, we tuned V_{gate} from -100 V to 90 V which enabled us to introduce hole densities of up to $p_{max} \approx 5.0 \times 10^{12}$ cm $^{-2}$ and electron densities of up to $n_{max} \approx 8.6 \times 10^{12}$ cm $^{-2}$. This asymmetry is caused by initial doping in the pristine flake which shifts the intrinsic Fermi level away from the Dirac point. The sample was placed in a cryostat at 11 K.

Fig. 5.4(a) shows selected spectra at different gate voltages, Fig. 5.4 (b) shows all spectra of one measurement cycle combined in a false-color-plot.

As predicted by theory (see chapter 4), it is evident that the G mode stiffens as charge carriers are introduced in the flake. The shift is not as symmetrical as one would expect; this is most likely due to adsorbates amassing on the flake as the measurement goes on, which create an increasing, statically charged background. At about -60 V, the lineshape of the G mode changes dramatically, becoming very broad. This is countermanded around 0 V.

In Fig. 5.5, both the position (black squares) and FWHM (blue circles) of the G mode at various gate voltages is plotted. The fast change in position between -100 V and -60 V is striking, starting at about 1592 cm $^{-1}$ and softening by more

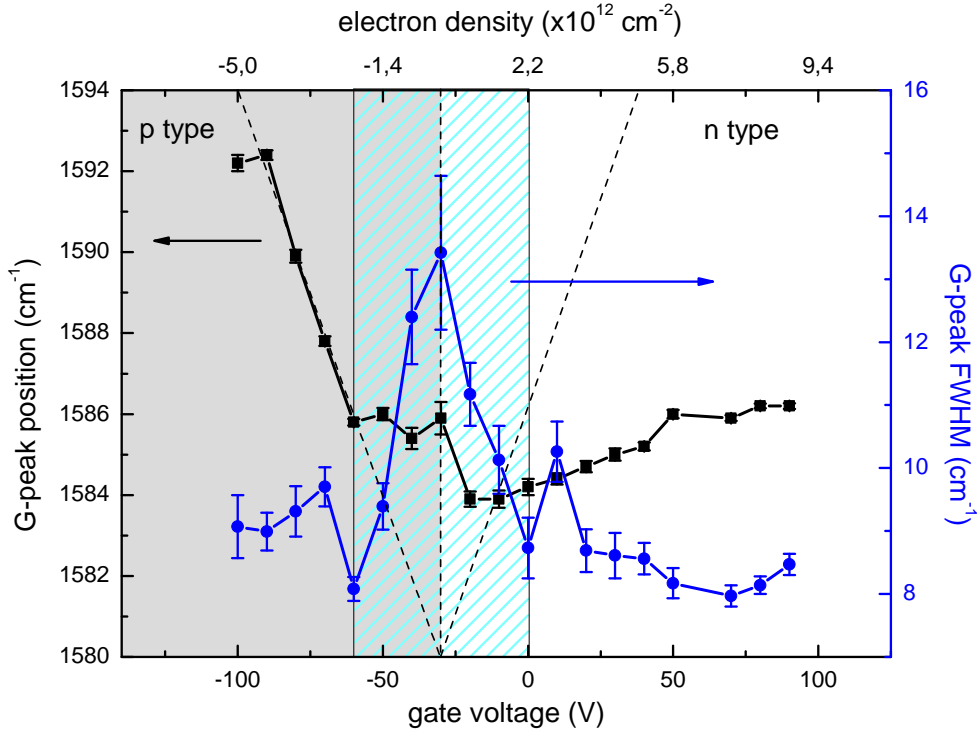


Figure 5.5: *G* peak position (black squares) and FWHM (blue circles) in relation to gate voltage and, hence, electron density. In the *p*-type doped region, the *G* peak shift nicely follows expectations (slanted dashed lines). In the *n*-type doped region, the position of the *G* peak stays below the expected shift. This is probably caused by a continuing increase of adsorbates during the measurement. The lineshape of the *G* mode is sharp outside and wide inside the Landau damping regime (area with light blue hatching). The vertical dashed line marks charge neutrality.

than 6 cm^{-1} . Between -60 V and 0 V , the static charged background localized on the flake dominates the spectra, pinning the *G* peak position around 1585 cm^{-1} , but between 0 V and 90 V the *G* band stiffens again, albeit at a smaller rate than before, which we attribute to a growing number of adsorbates on the flake. The lineshape behaves as predicted with a FWHM of about 8 cm^{-1} outside and more than 13 cm^{-1} within the Landau damping regime, marked by the hatched area in Fig. 5.5.

From this, we conclude that a backgate voltage of -30 V was required in this sample to shift the Fermi level to the Dirac point. Taking into consideration that the gate voltage V_{gate} relates to the number of holes as $p \approx 7.2 \times 10^{10} \text{ cm}^{-2} \times (V_{gate} - V_{Dirac})$, when V_{Dirac} is the backgate voltage necessary to shift the Fermi level to the charge-neutrality point (see also chapter 4), we conclude that the initial doping in the flake after exfoliation and contact evaporation was about $n \approx 2.2 \times 10^{12} \text{ cm}^{-2}$. V_{Dirac} is marked by a vertical dotted line in Fig. 5.5.

The tilted dotted lines mark the expected shift of the G peak dependent on the number of charges in the flake. Their slope corresponds to a shift of 1 cm^{-1} for every $4.5 \times 10^{11} \text{ cm}^{-2}$, starting at 1580 cm^{-1} for undoped graphene. The measurements on the p-type doped branch comply very nicely with this prediction, but, as mentioned before, not so on the n-type doped side. This is most likely due to adsorbates.

The 2D peak could not be observed in single layer graphene due to losses on the cryostat window. From the literature [Das08] it is known, that the 2D peak is not expected to change in shape or position at the charge carrier densities reached in our setup.

5.3 P-type doping in single layer graphene with circular antidots

In this section, we will discuss the influence of circular antidots conditioned by EBL and RIE (see chapter 4) on the Raman spectra of single layer graphene. We have found a stiffening and sharpening of the G mode on the antidot lattices when compared to unpatterned graphene and attribute this to a p-type doping in the patterned areas. The results presented here were previously published in Ref. [Hey10].

We have prepared four graphene flakes with antidot lattices, each with a different lattice constant ranging from 80 nm to 400 nm, but always with the same diameter of 60 nm. The series of samples also includes two antidot lattices with smaller diameters (50 nm) in single layer graphene. We will discuss the D, G and 2D modes observed on these samples in terms of peak position, peak width and peak intensity.

Fig. 5.6(a) shows a microscope image of sample circAD80, which consists mostly of a single layer with some graphite attached at the bottom left. The contours of both the single layer part and the graphite have been highlighted in white. The former has been etched with circular antidots arrayed in two rectangles following the procedure described in chapter 4 with 80 nm lattice constant. The dashed black rectangles in the graph indicate the patterned areas. In the region marked A, the diameter of the antidots is 50 nm, in B, 60 nm. Region R was left unpatterned as reference section. Figs. 5.6(b) and (c) show SEM images of the antidots in regions A and B, respectively. Fig. 5.6(d) shows spectra taken in regions A, B, and R. In region R, the defect-induced D and D' peak amplitudes are minimal, while the G and 2D modes dominate. In regions B and A, artificial defects are introduced via the antidot lattices. This leads to a significant increase in the D and D' bands and a decrease in the G and 2D bands. The increase of the defect-induced modes is owed to the amount of defects along the antidot edges.

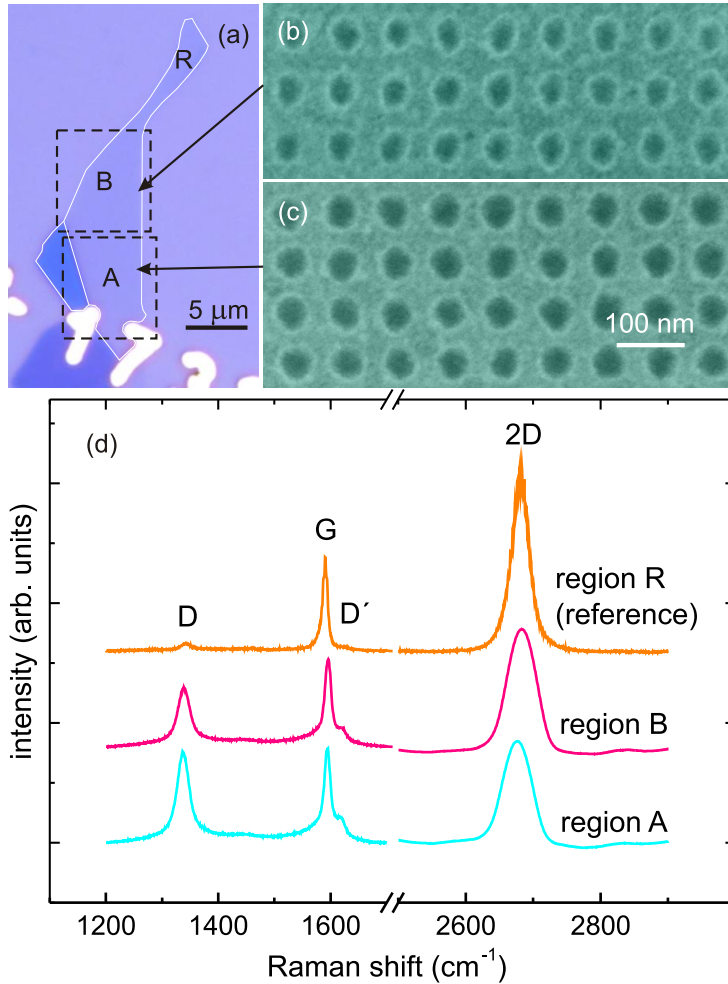


Figure 5.6: (a) microscope image of sample *circAD80*. The flake has been outlined in white, detailing the single layer portion, the antidot lattices are marked by dashed black rectangles. In both cases, the antidot lattice has 80 nm lattice constant, in area A the antidot diameter is 60 nm, in area B 50 nm. Area R was left unpatterned as reference section. (b) and (c) SEM image of the antidot lattice in area B and A, respectively. (d) Single spectra taken on area A, B, and R, respectively. Note, that the intensity of the D and D' peaks is strongly linked to the size of the antidots and thus to the amount of defects in the sample.

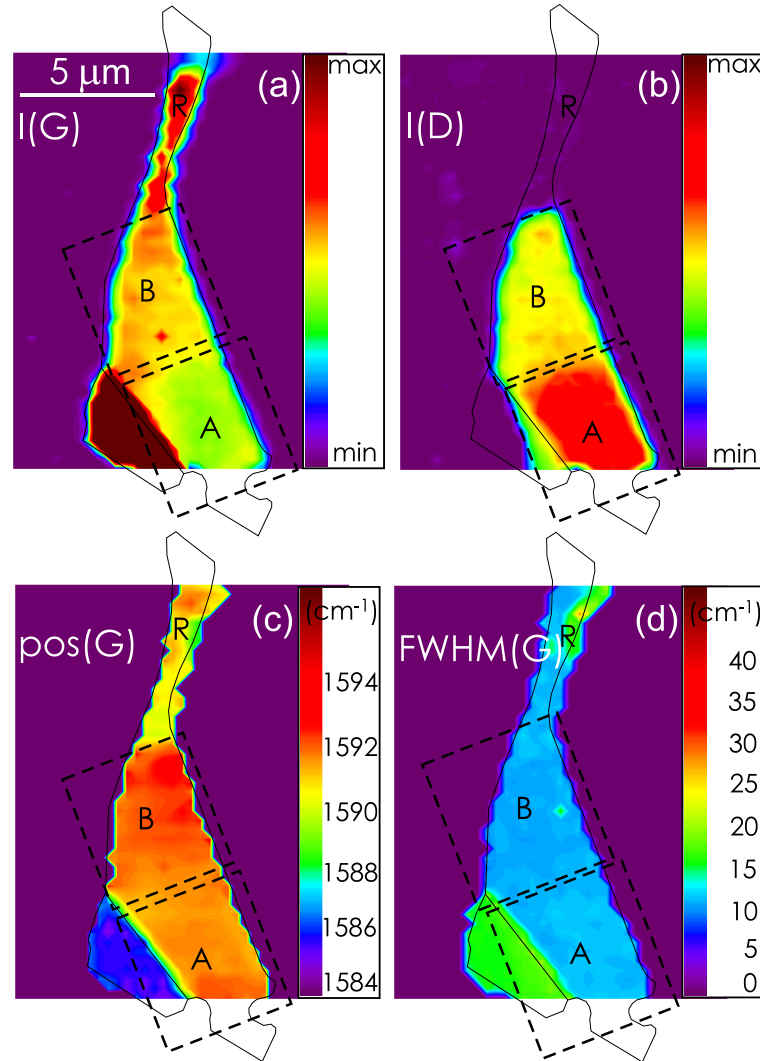


Figure 5.7: False color images of a Raman scan of sample circAD80 detailing (a) the intensity of the G mode, (b) the intensity of the D mode, (c) the position of the G mode, and (d) the FWHM of the G mode. The outline of the flake is sketched in black, the positions of the antidot lattices are marked by dashed black rectangles. (a) The intensity of the G peak follows the topology of the flake, being highest in the reference section R and lowest in area A with the large antidots. (b) The intensity of the D mode follows the amount of defects in the flake with highest intensity in region A with the larger antidots, lower intensity in region B with smaller antidots and no intensity in the reference section R. (c) Surprisingly, the position of the G mode is up-shifted on the antidot lattices by about 3 to 5 wavenumbers with respect to the reference section. (d) FWHM(G) is uniformly sharp over the whole flake, attesting to the high crystalline quality of the sample.

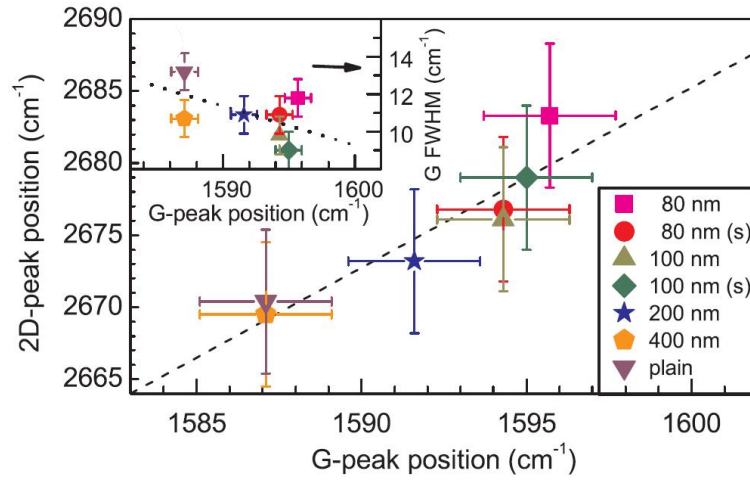


Figure 5.8: Plot of the energetic positions of the observed 2D modes versus the positions of the G modes of all investigated antidot samples. The legend indicates the period of the antidot lattices. Antidot diameter was usually 60 nm, those samples with 50 nm antidot diameter are denoted (s). See text for explanation of the dashed line. The inset shows the linewidths of the G modes versus energetic position. The dotted line in the inset is a guide to the eye.

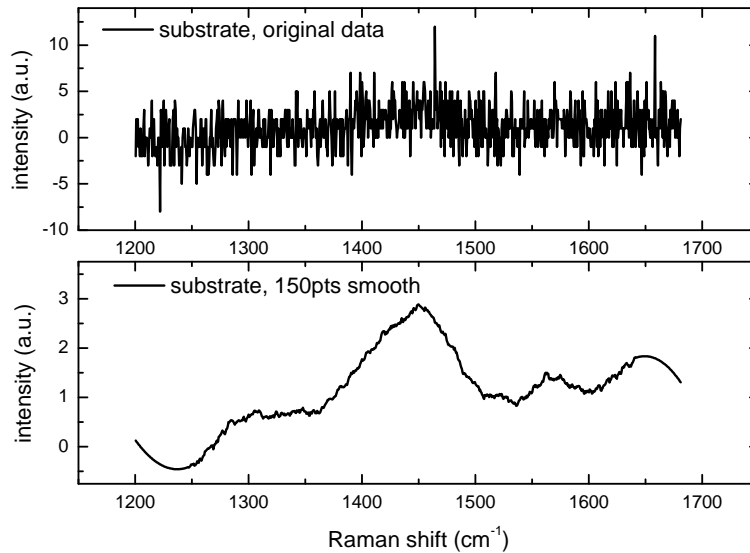


Figure 5.9: spectrum of the Si/SiO₂ substrate, collected next to flake circAD80, plain data on top, 150 points smooth on bottom. Both spectra exhibit a weak feature at about 1450 cm⁻¹.

Since the antidots in region A are larger than in region B and thus have a longer edge, resulting in more defects per square unit, the intensity of the D and D' peaks is larger in region A than in region B. The loss in intensity of the G and 2D bands is due to the diminished amount of graphene in regions A and B. Again, the intensity is lowest in region A with the larger antidots and consequently least graphene.

We performed a Raman scan on sample circAD80. In Fig. 5.7, false-color plots representing several aspects of this Raman scan are assembled. Both the outline of the flake and of the antidots lattices, as introduced in Fig. 5.6(a), are repeated to show the placement of the flake during the scan. The color scale is explained on the right. The scale bar of $5 \mu\text{m}$ in 5.7(a) is true for all false-color plots shown here.

Fig. 5.7(a) plots the intensity of the G mode and thus essentially reproduces the topology of the whole flake. The intensity of the G band increases from region A, which contains the larger holes, to region B, with the smaller holes, to the unpatterned reference section R. A maximum intensity is found in the graphite part on the bottom, left of region A. On the other hand, a pronounced intensity of the D mode is observed in the antidot areas A and B with higher intensities in A, which contains the larger holes with longer edges (Fig. 5.7(b)). Interestingly, the position of the G peak is systematically higher in the antidot lattices than in the reference part, see Fig. 5.7(c). While the G peak energy is about 1589 cm^{-1} in region R, it is upshifted by 3 or 5 cm^{-1} , respectively, to about 1592 cm^{-1} in region B and to about 1594 cm^{-1} in region A.

Fig. 5.7(d) shows the linewidth of the G mode. $\text{FWHM}(\text{G})$ is between about 9 and 11 cm^{-1} in the whole flake, comparable to pristine graphene samples [Cas07], [Cas09a], and to plain gated graphene outside the Landau damping region, see section 5.2, attesting to the high crystalline quality of the flake. In significantly disordered samples, linewidths in the range of several tens of wavenumbers are expected [Cas09a]. This clearly excludes the interpretation that the observed G mode stiffening in the antidot lattice is caused by disorder. Rather, the narrow and almost unchanged linewidths favor the explanation, that doping is the reason for the stiffening, caused by the nonadiabatic removal of the Kohn anomaly (see chapter 3).

As described in chapter 3, it is possible to discern electron and hole doping in graphene by comparing the positions of the G and 2D peaks. This was done in Fig. 5.8 for all single layer samples in this series, summarizing the most important results of this section in Fig. 5.8. If we plot, sample by sample, the positions of the observed 2D modes versus the positions of the G modes, we find an approximately linear correlation. The linewidths of the observed G modes in the different samples tentatively decrease with increasing G mode energy, see inset of Fig. 5.8. The correlation between G mode and 2D mode positions was investigated systematically on a large number of single layer graphene samples, both, in as-deposited and in gated samples [Cas09a], [Das08]. It was reported that while the 2D mode

position *decreases* with increasing G mode position in n-doped samples, it *increases* with increasing G mode position in p-doped samples. The dashed line in Fig. 5.8 indicates, for the range of G mode energies relevant for our work, the slope of the approximately linear correlation, as reported in Ref. [Cas09a] for p-doped graphene. In stark contrast, for n-type doping, the slope should be negative. One can see a fairly good agreement of the data, extracted from our measurements on the antidot samples, with the dashed line in Fig. 5.8. Please note that the 2D mode energies in our experiment are slightly lower than in Ref. [Cas09a], since we measured with a 532 nm line, as opposed to a 514 nm line in Ref. [Cas09a]. The 2D mode energy increases with decreasing laser wavelength due to the double-resonant intervalley scattering process described in chapter 3. Therefore, the dashed line in Fig. 5.8 is rigidly shifted by about 17 cm^{-1} to lower energies as compared to 2D mode energies in Fig. 3 of Ref. [Cas09a]. Obviously, our data in Fig. 5.8 suggest a p-type doping of the antidot lattices. Please note, that in previous Raman investigations of graphene flakes also indications of a stronger p doping in close vicinity to the edges, as compared to the bulk of the samples, were found [Cas09b], sometimes even though the bulk of the sample was n-type doped [Kar11]. Hence, the amount of p doping appears to increase systematically with the ratio of etched to unetched graphene area, which is tentatively verified by the data in Fig. 5.8. As a result, the plain reference sample regions are not affected by the doping.

In order to quantify the amount of p doping, we compare the results on the antidot samples to measurements on an unpatterned gated sample, presented in the first section of this chapter. As stated there, the slope of the shift of the G mode position corresponds to a shift of 1 cm^{-1} for every $4.5 \times 10^{11} \text{ cm}^{-2}$ increase in hole density, starting at 1580 cm^{-1} for undoped graphene. Of course, this relation holds for charge carrier densities $> 1 \times 10^{12} \text{ cm}^{-2}$, above the disorder-dominated regime, only. With this calibration, we can assign hole densities between about $3 \times 10^{12} \text{ cm}^{-2}$ in circAD400 and $7 \times 10^{12} \text{ cm}^{-2}$ in circAD80.

It is difficult to ascertain the origin of the observed p-type doping. The preparation process of the antidots involving RIE and EBL certainly contaminates the flakes [Fan11], but this alone can not cause the entire doping, as doping has been observed at the edges of pristine flakes [Cas09b]. Nanoperforated graphene samples have been reported to have p-type doping [Kim12], despite special care to avoid contamination of the samples. Kim et al. employed a sacrificial polymer buffer layer to protect the graphene during etching, but still found p-type doping. It is not possible to compare doping levels to the antidot samples presented here, as Kim et al. only give the width of the graphene ribbon between etched nanoperforations and neither the diameter of the perforations nor the lattice constant, but as the ribbon widths are given as 13.1 nm and 7.5 nm with comparatively large perforations, it is safe to assume, that more defects were introduced in the nanoperforated samples in [Kim12] than in the antidot samples presented here. The G peak positions in [Kim12] are given as 1586 cm^{-1} and 1593 cm^{-1} , correspond-

ing to charge carrier densities of $2.7 \times 10^{12} \text{cm}^{-2}$ and $5.9 \times 10^{12} \text{cm}^{-2}$, respectively, which, considering the large amount of edges in the nanoperforated samples, can be taken as a reduction in charge carrier density per unit edge length when compared to the samples presented here due to the careful sample treatment, but the nanoperforated graphene was still p-type doped. Kim et al. attribute the doping to dangling oxygen bonds [Kim12], however, Begliarbekov et al. reduced several graphene antidot lattices using L-ascorbic acid and found no change to the doping observed in the samples before reduction [Beg11], so oxygen appears ruled out as dopant. Another possible source for doping is hydrogen. Strong hydrogen contamination should lead to C-H bonds, which leave a signature in the Raman spectrum at about 1450cm^{-1} [Sta11]. The spectra in 5.6 (c) show a very weak feature at 1450cm^{-1} , which indeed appears to be strongest in region A, where the most doping was observed, and weakest in the reference section. However, this feature may also be observed on plain Si/SiO₂ wafers and could be attributed to a third overtone of the Si-mode at about 500cm^{-1} , too. Fig. 5.9 shows a spectrum collected on the plain substrate next to flake circAD80. The top spectrum displays the unaltered data, the spectrum on the bottom is the result of a 150-point-smooth using the Savitzky-Golay algorithm. Both spectra exhibit a weak peak at 1450cm^{-1} .

In summary, p-type doping at graphene edges has been reported several times in the literature [Hey10] [Beg11] [Kar11] [Kim12], but the origin of the doping is still unclear. It appears unlikely that oxygen is the dopant, hydrogen appears more likely, but is not ascertained so far. The only thing that appears certain at this point is, that graphene on Si/SiO₂ possesses edge states, increasing the charge carrier density at the edge [Wim08] and causing p-type doping.

5.4 Raman study of anisotropically etched hexagonal antidots in single layer graphene

We studied a crystallographic etching process of antidots in single layer graphene by Raman spectroscopy. Sample hexAD400/200 was subjected to successive steps of exfoliation, patterning with circular antidots using EBL and RIE, a preconditioning step and two consecutive anisotropic etching steps, turning the circular into larger, hexagonal antidots with predominantly zigzag edges. For a more detailed description of the sample preparation, see chapter 4. Each step was documented by Raman spectroscopy covering the D and G mode in a first and the 2D mode in a second scan. SEM images were deferred until the last Raman scan was completed to avoid dirtying the sample. We compared the D mode intensity to the length of edges illuminated to discern armchair from zigzag edges and found the hexagonal antidots to sport mostly zigzag chirality. For the influence of the

edge chirality on the D mode intensity, see chapter 3.

We used a graphene flake with an unusually large single layer part to monitor the evolution of circular into hexagonal antidots via Raman spectroscopy. Fig. 5.10(a) shows a microscope image of the flake with contours highlighted in white. Areas A and B were to be patterned with antidot lattices, area R was kept unpatterned as reference section. Fig. 5.10(b) shows an SEM image of area B after the second, final anisotropic etching step. The antidots have acquired a pronounced angular shape comprised of straight edges, forming recognizable hexagons in many cases. An AFM image of the whole flake after the last etching step was completed may be seen in Fig. 5.10(c). The antidot lattice constant in area A is 400 nm, area R was left unpatterned, and the lattice constant of area B is 200 nm, half that of area A. A fold in the graphene runs through area B, which results in local strain and thus a possible shift in G and 2D peak positions, additionally to any doping-induced shift, in spectra taken on this crease. As we are mostly concerned with the intensity of the D peak, this will not touch our discussion. Also, if single spectra, as opposed to scans, were evaluated, care was taken to avoid the neighborhood of this crease. The schematic in Fig. 5.10(d) shows the graphene lattice arranged to form an ideal hexagonal antidot with pure zigzag edges. Note that even in a perfect antidot, the corners of the hexagon cannot follow the zigzag chirality completely.

We performed Raman scans on this flake after exfoliation and after every successive patterning step. Fig. 5.11 shows a compendium of these measurements. For this, false color images depicting the D and G peak intensity, respectively, of the pristine flake after exfoliation, of the flake with circular antidots after EBL and RIE, and of the flake with hexagonal antidots after the final anisotropic etching step were chosen. The sketches in the first line illustrate the status of the flake in each column, in the second (third) line, the D (G) mode intensity is shown. In each row, minimum and maximum value for the false-color images was kept constant to allow easy comparison. Minimum value was zero in all cases. The color scale used may be found on the right. The $5\ \mu\text{m}$ scale bar shown in the first image of each row is valid for all false-color plots.

In the pristine flake, a D peak is expected only at the edges. It is so weak that in the image displayed in Fig. 5.11, it does not register at all due to the color scale employed. In the next image, however, the D peak is clearly visible. It is most prominent in area B where the antidot lattice constant is 200 nm, and weaker in area A, where the antidot lattice constant is 400 nm. In the reference section R, the D peak is very weak. In the last image in this row reproducing the flake after the second anisotropic etching step, the D peak is greatly diminished in both areas A and B. Its intensity is approximately halved in area B and too small to clearly register in area A. This reduction of the D peak is exactly what one would expect from antidots with mostly zigzag edges. The remaining D peak intensity can be attributed to atoms breaking the pure zigzag chirality at the corners of the antidots and at not perfectly etched hexagons. The G peak intensity shown

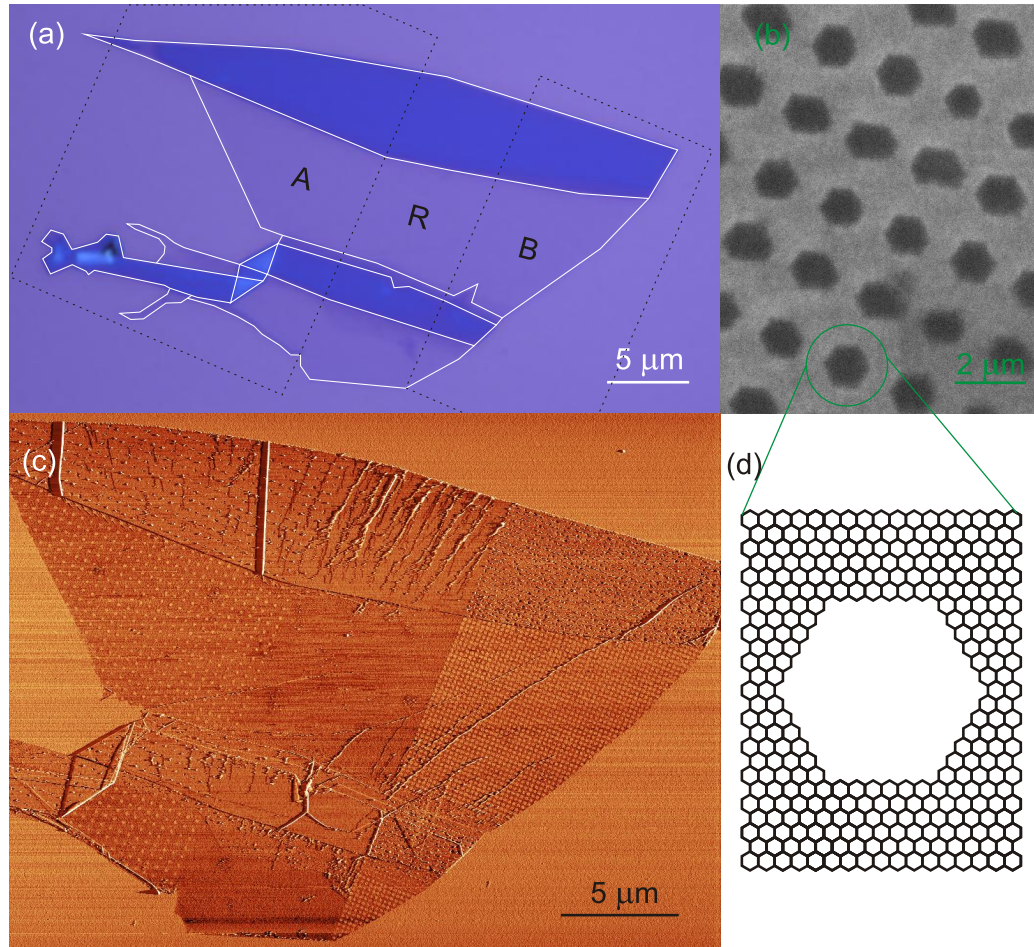


Figure 5.10: (a) optical microscope image of sample hexAD200/400. Contours of the flake are highlighted in white. The middle section is single layer graphene. The antidot lattice in area A has 400 nm, in area B 200 nm lattice constant. Area R was left unstructured as reference section. (b) SEM image of part of area B, after the second anisotropic etching step and the last Raman scan. The antidots have acquired a noticeably honeycomb-like shape. (c) AFM image of sample hexAD200/400, taken after the second anisotropic etching step and the last Raman scan. Note the antidot lattices in areas A and B and the crease in area B. (d) schematic of the graphene lattice around an anisotropically etched antidot. The anisotropic etching process results in predominantly zigzag edges, giving the antidots their distinctive hexagonal shape.

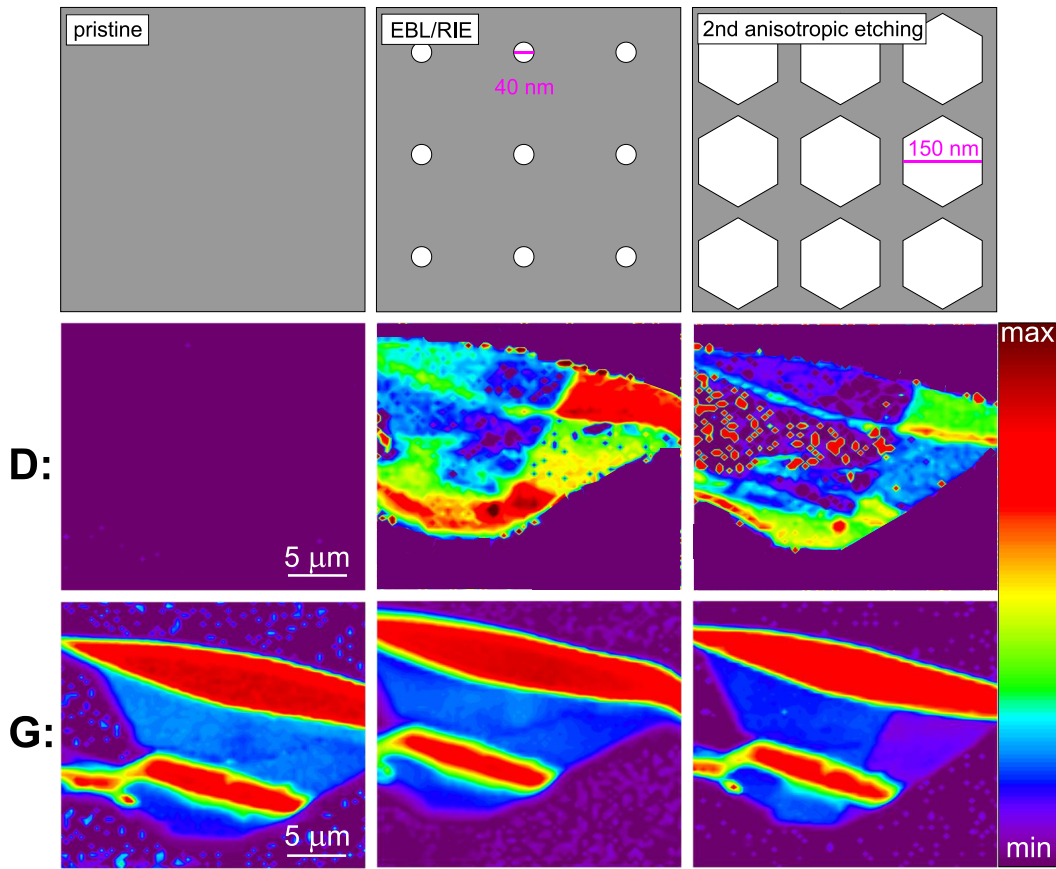


Figure 5.11: Three of the processing steps sample hexAD200/400 was subjected to, and subsequent Raman scans depicting the D and G peak intensity. First row: processing steps, second row: D peak intensity, third row: G peak intensity. First column: pristine flake, second column: flake after EBL and RIE, third column: flake after the final anisotropic etching step. The $5\ \mu\text{m}$ scale bars given in the first images of D and G peak intensity are valid for all false color plots. All false color plots of the D (G) peak have the same minimum and maximum values, therefore the color scale given on the right is valid for all scans of each peak. The D peak in pristine graphene is only existent along the edges of a flake. In this case it is too weak to register on the color scale employed. In the flake with circular antidots, the D peak is especially prominent in area B and appears noticeably weaker in area A. After the second anisotropic etching step, the D peak intensity in area B is greatly diminished. It is nearly null in areas A and R. The G peak intensity gives a topology of the flake. After the EBL and RIE steps, it is mildly diminished in areas A and B, after the final etching step, it is greatly diminished in area A and vanquished in area B.

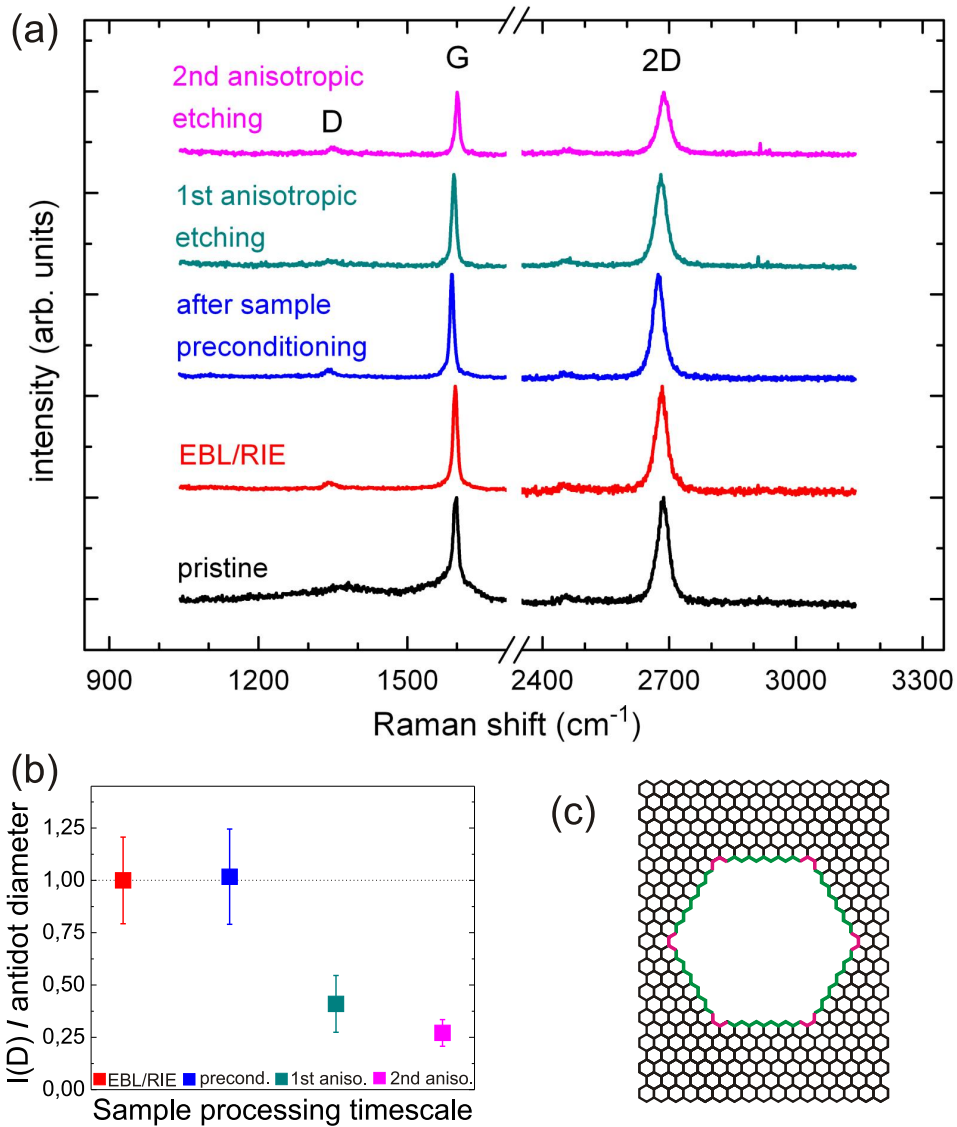


Figure 5.12: (a) single spectra recorded on area B of sample hexAD400/200 after exfoliation (black), patterning of the circular antidots (red), preconditioning (blue), the first (teal) and second (pink) anisotropic etching step. $I(D)$ diminishes strongly after the first anisotropic etching step and recovers slightly after the second anisotropic etching step. (b) Intensity of the D mode per unit edge length after each preparation step, excepting exfoliation. (c) schematic detailing the atomic configuration along a hexagonal antidot with perfect zigzag edges (green). Note, that even in a perfect antidot, the corners (pink) deviate from zigzag chirality. Therefore, an antidot with only zigzag edges is not possible.

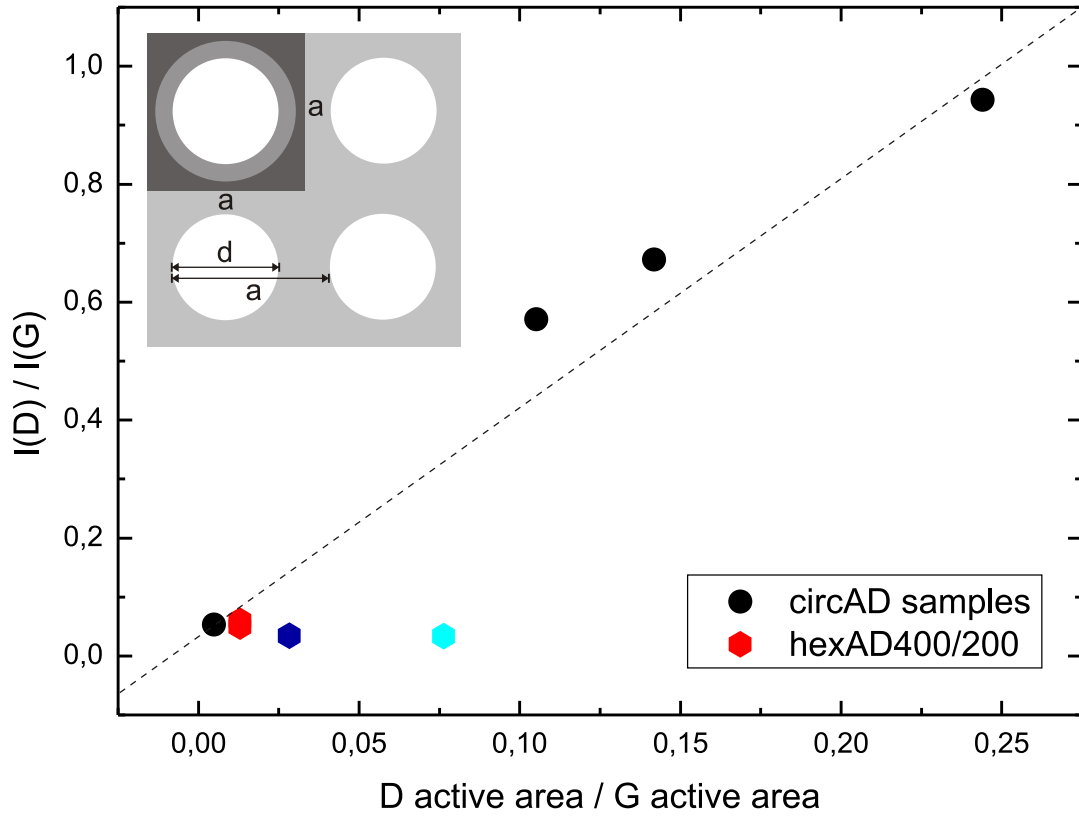


Figure 5.13: intensity ratio of D peak to G peak over ratio between areas on the graphene flake contributing to the D and G peak, respectively. Black circles denote data from single layer graphene with circular antidots, hexagonal data points stem from sample hexAD400/200 after EBL/RIE (red), preconditioning (red), first (dark blue) and second anisotropic etching step (light blue). The dashed line is a guide to the eye. The inset shows a schematic of an antidot flake illustrating the D active area (grey ring) and the G active area (grey ring plus dark grey square) with a the antidot lattice period and d the antidot diameter.

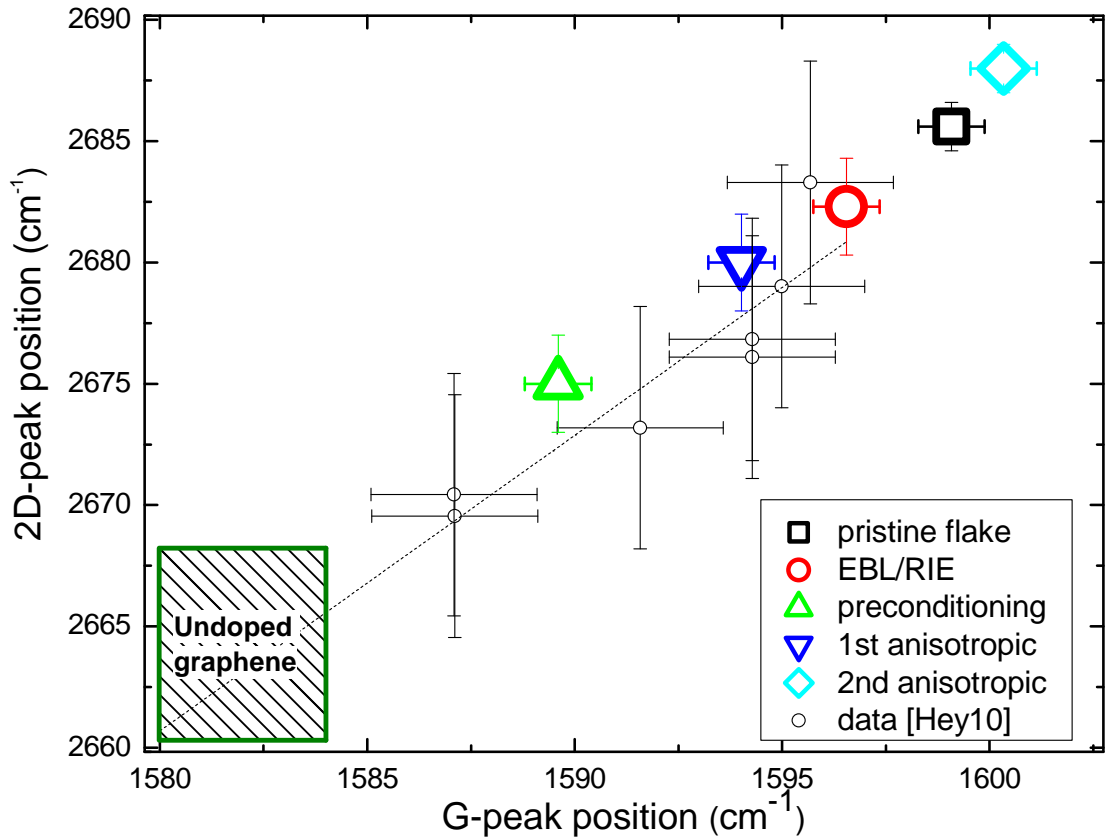


Figure 5.14: Plot of $Pos(2D)$ vs $Pos(G)$ after each etching step of sample *hexAD400/200*, in color. In gray, the data points of the circular antidot samples from Fig. 5.8 and [Hey10] are shown as reference. Dashed line as in Fig. 5.8 and [Hey10].

in the first image of the third row emulates the topology of the pristine flake, strongest on the multilayer parts and weaker on the single layer area. After EBL and RIE, the G peak intensity is slightly lower in areas A and B and unchanged in area R. In the last image, taken after the second anisotropic etching step, it is greatly diminished in area A and nearly vanished in area B. This indicates that the antidots have grown so big in the successive etching steps as to leave very little graphene in area B and only a little more in area A.

To shed more light on the effect of the individual process steps and to more closely follow the changes in the D peak, Fig. 5.12(a) shows single spectra taken on area B after each processing step. Care was taken to avoid the crease running through area B and to only compare spectra from the same spot on the flake in each scan. The spectra were originally recorded with different integration times (0.5 s, 1 s and 2 s). To account for this difference, the count numbers were multiplied by a correction factor (2, 1 and 0.5, respectively). The spectra show a pronounced D peak after patterning with circular antidots in successive EBL and RIE steps,

and after the preconditioning step. It is nearly vanquished after the first and recurs only slightly after the second anisotropic etching step. If we take a circular antidot to be constructed of approximately equal amounts of zigzag and armchair edges, this distinct reduction in the D peak intensity is an indication, that the anisotropic etching process strongly reduces the amount of armchair edges in the flake. As the intensity of the D peak in disordered edges is dependent on the number of defects i.e. the length of the edge illuminated, and the laser spot size, which is approximately 800 nm, is much larger than the lattice constant of either antidot lattice, it is useful to correlate the intensity of the D peak with the antidot diameter, as shown in Fig. 5.12(b). $I(D)/\text{antidot diameter}$ after EBL and RIE was set to one. From this graph, it is clearly evident, that the D peak intensity per unit edge length is greatly diminished after the first and even more after the second anisotropic etching. The apparent conflict between the absolute D peak intensity, which increases from the first to the second anisotropic etching step in 5.12(a), and the relative D peak intensity plotted in 5.12(b) is resolved when the large size of the antidots after the last etching step is taken into account.

Another way to illustrate the difference between circular antidots and anisotropically etched, hexagonal antidots is to compare, in several samples, the intensity ratio between D and G peak to the area ratio contributing to the D and G intensity, respectively.

In the area illuminated by the laser spot, all graphene present contributes to the G peak intensity, and the area activated by the G peak is therefore proportional to $a^2 - (\frac{d}{2})^2\pi$, when a denotes the distance between antidots, that is the lattice period, and d the diameter of an antidot. See upper inset of Fig. 5.13 for a schematic.

Contrary to the case of the G peak, only a small rim of about 4 nm width along the edge of an antidot contributes to the D peak intensity (see chapter 3). The size of this active rim is determined by the spatial extent of the process causing the D peak. As discussed in section 3.3.3, the D peak is caused by a triple- or double-resonant Raman scattering process. If this process is only double-resonant, one of the intermediate states violates energy conservation by $\hbar\omega_D \approx 170$ meV, which limits, together with the uncertainty principle, the duration of the process to $1/\omega_D \approx 3$ fs. Considering that electrons and holes move in graphene with the Fermi velocity $v_F \approx 1,1 \times 10^6$ m/s, the time-limit translates to a spatial extent of the D peak scattering process of 4 nm. Therefore, the D active area is proportional to a 4 nm-wide ring around an antidot, that is $\approx d\pi 4$ nm, with d the diameter of the antidot, see schematic in Fig. 5.13.

In Fig. 5.13, we plotted the ratio of D active area over G active area versus the ratio of D mode intensity over G mode intensity for the series of samples with circular antidots introduced in section 5.3 (black circles) and for each processing step in sample hexAD400/200. Thereby, red hexagons mark the sample after EBL/RIE and the preparation step, respectively, dark blue hexagons after the first and light blue hexagons after the second anisotropic etching step. In the

samples with circular antidots, the intensity ratio of D and G mode correlates linearly to the ratio of active areas, whereas in the anisotropically etched sample, the intensity ratio is much lower. This indicates, that most of the D active area in sample hexAD400/200 does not contribute to the D peak intensity, which can be understood as evidence that the antidot edges in the anisotropically etched sample are mostly zigzag.

From Fig. 5.12(b) and Fig. 5.13 we deduce, that the anisotropic etching step indeed distinguishes between different chirality and the resultant hexagonal antidots have predominantly zigzag edges.

In the previous section, we have found circular antidots to be p-type doped [Hey10]. This is also the case in sample hexAD400/200, as may be seen from Fig. 5.14. Following the same reasoning as in section 5.3, we have plotted the G peak position versus the 2D peak position of the spectra shown in Fig. 5.12(a) and have found the flake to be always p doped, to varying degrees. Especially the pristine flake (black square) was strongly doped. This results most likely from adsorbates on the flake surface as the sample had been stored under ambient conditions for several months after exfoliation before the first Raman measurements were made. The adsorbates are probably also responsible for the background between 1250 cm^{-1} and 1500 cm^{-1} in Fig. 5.12(a) in the pristine flake. This background is missing in all consecutive spectra, which suggests that the adsorbates were removed during the EBL and RIE steps. The doping, however, is found after each patterning step and, following the calibration assigned in section 5.3, ranges from about $4.5 \times 10^{12}\text{ cm}^{-2}$ after preconditioning to about $9 \times 10^{12}\text{ cm}^{-2}$ after the second anisotropic etching step.

The results presented in this section have been previously published in [Obe13], which contains additionally to Raman spectra weak localization measurements confirming our results, namely, that the anisotropically etched antidots have predominantly zigzag edges.

Chapter 6

Conclusion and outlook

This chapter summarizes the present work, listing again the samples, the observation technique, our observations and the conclusions we draw from them. The last two paragraphs of this chapter are concerned with possible avenues for future study in this field.

6.1 Conclusion

This work has concentrated on two issues: the effect that nanopatterning in the form of periodic antidot lattices has on graphene and the preparation of perfect zigzag edges. To test the first, we have prepared a series of samples of single layer graphene flakes with square antidot lattices with different lattice constants ranging from 80 nm to 400 nm and two types of antidot diameters (50 nm and 60 nm). Scanning Raman spectroscopy showed an increase of the D peak intensity and a decrease of the G peak intensity as well as a stiffening of the G mode position. The former are due to artificial introduction of defects and decrease of graphene per unit area by the antidots, respectively, while we attribute the latter to doping. Comparison of the positions of G and 2D modes let us determine the graphene antidot lattices to be p-type doped with charge carrier concentrations ranging from $3 \times 10^{12} \text{ cm}^{-2}$ in the 400-nm sample to $7 \times 10^{12} \text{ cm}^{-2}$ in the 80-nm sample.

Additionally, we have studied the preparation process of a large single layer graphene flake aimed at producing predominantly zigzag edges. We have patterned the flake with two types of square antidot lattices with 200 nm and 400 nm lattice constant, respectively, and subjected it to two anisotropic etching steps designed to selectively remove atoms at armchair sites, leaving clean zigzag edges

behind. The flake was processed in five steps - exfoliation from natural graphite, patterning of conventional antidots via electron beam lithography and reactive ion etching, a preparation step, and two anisotropic etching steps. After each step, we performed two Raman scans, one monitoring the D and G peak and one monitoring the 2D peak. Since the D peak probes intervalley scattering, which is forbidden for pure zigzag edges, we evaluated the D peak intensity for each step and have found the antidot edges to be predominantly zigzag after the anisotropic etching. Two anisotropic etching steps were performed to see if continued etching would increase the zigzag-to-armchair ratio and we have found this to be the case. Our results were also confirmed by weak localization measurements. We have also determined doping in the 200 nm antidot lattice and have found it to be p-type doped like the conventional antidots, ranging from $4.5 \times 10^{12} \text{ cm}^{-2}$ after the preconditioning step to $9 \times 10^{12} \text{ cm}^{-2}$ after the final anisotropic etching step.

6.2 Outlook

So far, we have prepared anisotropically etched antidots, but now that the process has been validated, other, more complicated shapes should also be possible. The next logical step is to prepare graphene nanoribbons with zigzag edges, as they are one step further on the road to spintronics. However, the main challenge in this area is to prepare the nanoribbon along the proper crystallographic direction in the flake. One possible approach could be to prepare a rectangular single layer flake by EBL and RIE and then etch it until a smaller, probably triangular ribbon along the proper crystallographic direction remains. Another approach is to first determine the crystallographic orientation of the flake by scanning Raman spectroscopy [You08] and then prepare a ribbon as close to the correct direction as possible. Anisotropic etching would then be employed to correct aberrations from the zigzag direction made in the RIE and EBL steps. The result should be an almost rectangular ribbon, which is presumably wider than usual nanoribbons in the first few attempts, but the procedure could probably be improved to create thin nanoribbons.

In addition to studying the effect of antidots on graphene, one could also be interested in the effect of antidot lattices on other two-dimensional materials, like MoS_2 . Preparing an array of graphene quantum dots for Raman study is also conceivable.

Bibliography

- [Bae12] S. Bae, H. Kim, Y. Lee, X. Xu, J.-S. Park, Y. Zheng, J. Balakrishnan, T. Lei, H. R. Kim, Y. I. Song, Y.-J. Kim, K. S. Kim, B. Özyilmaz, J.-H. Ahn, B. H. Hong, S. Iijima. “Roll-to-roll production of 30-inch graphene films for transparent electrodes”. *Nature Nanotechnology* **5**, 574–578 (2012)
- [Bal10] R. Balog, B. Jorgensen, L. Nilsson, M. Andersen, E. Rienks, M. Bianchi, M. Fanetti, E. Laegsgaard, A. Baraldi, S. Lizzit, Z. Sljivancanin, F. Besenbacher, B. Hammer, T. G. Pedersen, P. Hofmann, L. Hornekaer. “Bandgap opening in graphene induced by patterned hydrogen adsorption”. *Nature Materials* **9**, 315–319. ISSN 1476-1122 (2010)
- [Bas08] D. M. Basko. “Theory of resonant multiphonon Raman scattering in graphene”. *Physical Review B* **78**, 125418 (2008)
- [Bas09] D. M. Basko. “Calculation of the Raman G peak intensity in monolayer graphene: role of Ward identities”. *New Journal of Physics* **11**, 095011 (2009)
- [Beg11] M. Begliarbekov, O. Sul, J. Santanello, N. Ai, X. Zhang, E.-H. Yang, S. Strauf. “Localized States and Resultant Band Bending in Graphene Antidot Superlattices”. *Nano Letters* **11**, 1254–1258 (2011)
- [Ber06] C. Berger, Z. Song, X. Li, X. Wu, N. Brown, C. Naud, D. Mayou, T. Li, J. Hass, A. N. Marchenkov, E. H. Conrad, P. N. First, W. A. de Heer. “Electronic confinement and coherence in patterned epitaxial graphene”. *Science* **312**, 1191–1196 (2006)
- [Bla07] P. Blake, E. W. Hill, A. H. C. Neto, K. S. Novoselov, D. Jiang, R. Yang, T. J. Booth, A. K. Geim. “Making graphene visible”. *Applied Physics Letters* **91**, 063124 (2007)
- [Bor10] K. M. Borysenko, J. T. Mullen, E. A. Barry, S. Paul, Y. G. Semenov, J. M. Zavada, M. B. Nardelli, K. W. Kim. “First-principles analysis of electron-phonon interactions in graphene”. *Physical Review B* **81**, 121412(R) (2010)

- [Bri12] L. Britnell, R. V. Gorbachev, R. Jalil, B. D. Belle, F. Schedin, A. Mishchenko, T. Georgiou, M. I. Katnelson, L. Eaves, S. V. Morozov, N. M. R. Peres, J. Leist, A. K. Geim, K. S. Novoselov, L. A. Ponomarenko. “Field-Effect Tunneling Transistor Based on Vertical Graphene Heterostructures”. *Science* **335**, 947–950 (2012)
- [Cam09] L. C. Campos, V. R. Manfrinato, J. D. Sanchez-Yamagishi, J. Kong, P. Jarillo-Herrero. “Anisotropic Etching and Nanoribbon Formation in Single-layer Graphene”. *Nano Letters* **9**, 2600–2604 (2009)
- [Can04] L. G. Cançado, M. A. Pimenta, B. R. A. Neves, M. S. S. Dantas, A. Jorio. “Influence of the Atomic Structure on the Raman Spectra of Graphite Edges”. *Physical Review Letters* **93**, 247401 (2004)
- [Can11] L. G. Cançado, A. Jorio, E. H. M. Ferreira, F. Stavale, C. A. Achete, R. B. Capaz, M. V. O. Moutinho, A. Lombardo, T. S. Kulmala, A. C. Ferrari. “Quantifying defects in graphene via raman spectroscopy at different excitation energies”. *Nano Letters* **11**, 3190–3196 (2011)
- [Cas07] C. Casiraghi, S. Pisana, K. S. Novoselov, A. K. Geim, A. C. Ferrari. “Raman fingerprint of charged impurities in graphene”. *Applied Physics Letters* **91**, 233108 (2007)
- [Cas09a] C. Casiraghi. “Probing disorder and charged impurities in graphene by Raman spectroscopy”. *Physica Status Solidi RRL* **3**, 175–177 (2009)
- [Cas09b] C. Casiraghi, A. Hartschuh, H. Qjan, S. Piscanec, C. Georgi, A. Fasoli, K. S. Novoselov, D. M. Basko, A. C. Ferrari. “Raman Spectroscopy of Graphene Edges”. *Nano Letters* **9**, 1433–1441 (2009)
- [Che11] C. Chen, C. Park, B. W. Boudris, J. Horng, B. Gen, C. Firit, A. Zettl, M. F. Crommie, R. A. Segalman, S. G. Louie, F. Wang. “Controlling inelastic light scattering quantum pathways in graphene”. *Nature* **471**, 617 (2011)
- [Ci10] L. Ci, L. Song, C. Jin, D. Jariwala, D. Wu, Y. Li, A. Srivastava, Z. F. Wang, K. Storr, L. Balicas, F. Liu, P. M. Ajayan. “Atomic layers of hybridized boron nitride and graphene domains”. *Nature Materials* **9**, 430–435. ISSN 1476-1122 (2010)
- [Col11] J. N. Coleman, M. Lotya, A. O'Neill, S. D. Bergin, P. J. King, U. Khan, K. Young, A. Gaucher, S. De, R. J. Smith, I. V. Shvets, S. K. Arora, et al. “Two-dimensional nanosheets produced by liquid exfoliation of layered materials”. *Science* **331**, 568–571 (2011)
- [Das08] A. Das, S. Pisana, B. Chakraborty, S. Piscanec, S. K. Saha, U. V. Waghmare, K. S. Novoselov, H. R. Krishnamurthy, A. K. Geim, A. C. Ferrari, A. K. Sood. “Monitoring dopants by Raman scattering in an electrochemically top-gated graphene transistor”. *Nature Nanotechnology* **3**, 210–215 (2008)

- [Dat08] S. S. Datta, D. R. Strachan, S. M. Khamis, A. T. C. Johnson. “Crystallographic Etching of Few-Layer Graphene”. *Nano Letters* **8**, 1912–1915 (2008)
- [Dvo13] M. Dvorak, W. Oswald, Z. Wu. “Bandgap Opening by Patterning Graphene”. *Scientific Reports* **3**, 2289 (2013)
- [Eck12] A. Eckmann, A. Felten, A. Mishchenko, L. Britnell, R. Krupke, K. S. Novoselov, C. Casiraghi. “Probing the Nature of Defects in Graphene by Raman Spectroscopy”. *Nano Letters* **12**, 3925–3930 (2012)
- [Ero09] J. Eroms, D. Weiss. “Weak localization and transport gap in graphene antidot lattices”. *New Journal of Physics* **11**, 095021 (2009)
- [Fan11] J. Fan, J. M. Michalik, L. Casado, S. Roddaro, M. R. Ibarra, J. M. D. Teresa. “Investigation of the influence on graphene by using electron-beam and photolithography”. *Solid State Communications* **151**, 1574–1578 (2011)
- [Fan13] H. Fang, H. A. Bechtel, E. Plis, M. C. Martin, S. Krishna, E. Yablonovitch, A. Javey. “Quantum of optical absorption in two-dimensional semiconductors”. *Proceedings of the National Academy of Sciences of the United States of America* **110**, 29 (2013)
- [Fer06] A. C. Ferrari, J. C. Meyer, V. Scardaci, C. Casiraghi, M. Lazzeri, F. Mauri, S. Piscanec, D. Jiang, K. S. Novoselov, S. Roth, A. K. Geim. “Raman Spectrum of Graphene and Graphene Layers”. *Physical Review Letters* **97**, 187401 (2006)
- [Fer13] A. C. Ferrari, D. M. Basko. “Raman spectroscopy as a versatile tool for studying the properties of graphene”. *Nature Nanotechnology* **8**, 235–246 (2013)
- [Gao09] L. Gao, W. Ren, B. Liu, Z.-S. Wu, C. Jiang, H.-M. Cheng. “Crystallographic Tailoring of Graphene by Nonmetal SiO_x Nanoparticles”. *Journal of the American Chemical Society* **131**, 13934–13936 (2009)
- [Gon01] J. Gonzalez, F. Guinea, M. A. H. Vozmediano. “Electron-electron interactions in graphene sheets”. *Physical Review B* **63**, 134421 (2001)
- [Gra07] D. Graf, F. Molitor, K. Ensslin, C. Stampfer, A. Jungen, C. Hierold, L. Wirtz. “Spatially Resolved Raman Spectroscopy of Single- and Few-Layer Graphene”. *Nano Letters* **7**, 238–242 (2007)
- [Gui10] F. Guinea, M. I. Katnelson, A. K. Geim. “Energy gaps and a zero-field quantum Hall effect in graphene by strain engineering”. *Nature Physics* **6**, 30–33 (2010)
- [Gup06] A. Gupta, G. Chen, P. Joshi, S. Tadigadapa, P. C. Eklund. “Raman Scattering from High-Frequency Phonons in Supported n-Graphene Layer Films”. *Nano Letters* **6**, 2667–2673 (2006)

- [Han07] M. Y. Han, B. Ozyilmaz, Y. Zhang, P. Kim. "Energy Band-Gap Engineering of Graphene Nanoribbons". *Physical Review Letters* **98**, 206805 (2007)
- [Han12] T.-H. Han, Y. Lee, M.-R. Choi, S.-H. Woo, S.-H. Bae, B. H. Hong, J.-H. Ahn, T.-W. Lee. "Extremely efficient flexible organic light-emitting diodes with modified graphene anode". *Nature Photonics* **6**, 105–110 (2012)
- [Her08] Y. Hernandez, V. Nicolosi, M. Lotya, F. M. Blighe, Z. Sun, S. De, I. T. McGovern, B. Holland, M. Byrne, Y. K. Gunko, J. J. Boland, P. Niraj, G. Duesberg, S. K. K. Goodhue, J. Hutchison, V. Scardaci, A. C. Ferrari, J. N. Coleman. "High-yield production of graphene by liquid-phase exfoliation of graphite". *Nature Nanotechnology* **3**, 563–568 (2008)
- [Her12] F. Herziger, P. May, J. Maultzsch. "Layer-number determination in graphene by out-of-plane phonons". *Physical Review B* **85**, 235447 (2012)
- [Hey10] S. Heydrich, M. Hirmer, C. Preis, T. Korn, J. Eroms, D. Weiss, C. Schüller. "Scanning Raman spectroscopy of graphene antidot lattices: Evidence for systematic p-type doping". *Applied Physics Letters* **97**, 043113 (2010)
- [Hic13] J. Hicks, A. Tejada, A. Taleb-Ibrahimi, M. S. Nevius, F. Wang, K. Shepperd, J. Palmer, F. Bertran, P. Le Fevre, J. Kunc, W. A. de Heer, C. Berger, E. H. Conrad. "A wide-bandgap metal-semiconductor-metal nanostructure made entirely from graphene". *Nature Physics* **9**, 49–54. ISSN 1745-2473 (2013)
- [Kar11] J. Karch, C. Drexler, P. Olbrich, M. Fehrenbacher, M. Hirmer, M. M. Glazov, S. A. Tarasenko, E. L. Ivchenko, B. Birkner, J. Eroms, D. Weiss, R. Yakimova, S. Lara-Avila, S. Kubatkin, M. Ostler, T. Seyller, S. D. Ganichev. "Terahertz Radiation Driven Chiral Edge Currents in Graphene". *Physical Review Letters* **107**, 276601 (2011)
- [Kat07] M. I. Katnelson. "Graphene: carbon in two dimensions". *materials today* **10**, 20–27 (2007)
- [Kim11] K. Kim, Z. Lee, B. D. Malone, K. T. Chan, B. Aleman, W. Regan, W. Gannett, M. F. Crommie, M. L. Cohen, A. Zettl. "Multiply folded graphene". *Physical Review B* **83**, 245433 (2011)
- [Kim12] M. Kim, N. S. Safron, E. Han, M. S. Arnold, P. Gopalan. "Electronic transport and raman scattering in size-controlled nanoporated graphene". *ACS Nano* **6**, 9846–9854 (2012)
- [Koc12] S. Kochmann, T. Hirsch, O. S. Wolfbeis. "Graphene in chemical sensors and biosensors". *TrAC, Trends in Analytical Chemistry* **39**, 87–113 (2012)
- [Koh59] W. Kohn. "Image of the Fermi Surface in the Vibration Spectrum of a Metal". *Physical Review Letters* **2**, 393–394 (1959)

- [Kor11] T. Korn, S. Heydrich, M. Hirmer, J. Schmutzler, C. Schüller. “Low-temperature photocarrier dynamics in monolayer mos_2 ”. *Applied Physics Letters* **99**, 102109 (2011)
- [Kra10] B. Krauss, P. Nemes-Incze, V. Skakalova, L. P. Biro, K. von Klitzing, J. H. Smet. “Raman Scattering at Pure Graphene Zigzag Edges”. *Nano Letters* **10**, 4544–4548 (2010)
- [Kui11] T. Kuila, S. Bose, P. Khanra, A. K. Mishra, N. H. Kim, J. H. Lee. “Recent advances in graphene-based biosensors”. *Biosensors and Bioelectronics* **26**, 4637–4648 (2011)
- [Kür02] J. Kürti, V. Zolyomi, A. Grüneis, H. Kuzmani. “Double resonant Raman phenomena enhanced by van Hove singularities in single-wall carbon nanotubes”. *Physical Review B* **65**, 165433 (2002)
- [Lan28] G. Landsberg, L. Mandelstam. “Eine neue Erscheinung bei der Lichtzerstreuung in Krystallen”. *Naturwissenschaften* **16**, 557–558 (1928)
- [Lan37] L. D. Landau. “Zur Theorie der Phasenumwandlungen II”. *Physikalische Zeitschrift der Sowjetunion* **11**, 26–35 (1937)
- [Laz06] M. Lazzeri, F. Mauri. “Nonadiabatic Kohn Anomaly in a Doped Graphene Monolayer”. *Physical Review Letters* **97**, 266407 (2006)
- [Li09] X. Li, W. Cai, J. An, S. Kim, J. Nah, D. Yang, R. Piner, A. Velamakanni, I. Jung, E. Tutuc, S. K. Banerjee, L. Colombo, R. S. Ruoff. “Large-Area Synthesis of High-Quality and Uniform Graphene Films on Copper Foils”. *Science* **324**, 1312–1314 (2009)
- [Li10a] G. Li, A. Luican, J. L. dos Santos, A. H. C. Neto, A. Reina, J. Kong, E. Y. Andrei. “Observation of Van Hove singularities in twisted graphene layers”. *Nature Physics* **6**, 109–113 (2010)
- [Li10b] W. Li, M. Zhao, Y. Xia, Y. Mu. “Hydrogen saturation stabilizes vacancy-induced ferromagnetic ordering in graphene”. *Physical Chemistry Chemical Physics* **12**, 13699–13706 (2010)
- [Lia10] L. Liao, Y.-C. Lin, M. Bao, R. Cheng, J. Bai, Y. Li, Y. Qu, K. L. Wang, Y. Huang, X. Duan. “High-speed graphene transistor with a self-aligned nanowire gate”. *Nature* **467**, 305–308 (2010)
- [Lin10a] Y.-M. Lin, C. Dimitrakopoulos, K. A. Jenkins, D. B. Farmer, H.-Y. Chiu, A. Grill, P. Avouris. “100-GHz Transistors from Wafer-Scale Epitaxial Graphene”. *Science* **327**, 5966 (2010)
- [Lin10b] X. Ling, L. Xie, Y. Fang, H. Xu, H. Zhang, J. Kong, M. S. Dresselhaus, J. Zhang, Z. Liu. “Can Graphene be used as a Substrate for Raman Enhancement”. *Nano Letters* **10**, 553–561 (2010)

- [Lin11] Y.-M. Lin, A. Valdes-Garcia, S.-J. Han, D. B. Farmer, I. Meric, Y. Sun, Y. Wu, C. D. A. Grill, P. Avouris, K. A. Jenkins. “Wafer-Scale Graphene Integrated Circuit”. *Science* **332**, 1294–1297 (2011)
- [Maf07] D. L. Mafra, G. Samsonidze, L. M. Malard, D. C. Elias, J. C. Brant, F. Plentz, E. S. Alves, M. A. Pimenta. “Determination of la and to phonon dispersion relations of graphene near the Dirac point by double resonance Raman scattering”. *Physical Review B* **76**, 233407 (2007)
- [Mak10] K. F. Mak, C. Lee, J. Hone, J. Shan, T. F. Heinz. “Atomically thin mos₂: A New Direct-Gap Semiconductor”. *Physical Review Letters* **105**, 136805 (2010)
- [Mal09] L. M. Malard, M. A. Pimenta, G. Dresselhaus, M. S. Dresselhaus. “Raman spectroscopy in graphene”. *Physics Reports* **473**, 51–87 (2009)
- [Mar83] R. M. Martin, L. M. Falicov. *Light scattering in solids I*. Springer Verlag (1983)
- [Mar08] J. Martin, N. Akerman, G. Ulbricht, T. Lohmann, J. H. Smet, K. v. Klitzing, A. Yacoby. “Observation of electron-hole puddles in graphene using a scanning single-electron transistor”. *Nature Physics* **4**, 144–148 (2008)
- [Mau04a] J. Maultzsch, S. Reich, C. Thomsen. “Double-resonant Raman scattering in graphite: Interference effects, selection rules and phonon dispersion”. *Physical Review B* **70**, 155403 (2004)
- [Mau04b] J. Maultzsch, S. Reich, C. Thomsen, H. Requardt, P. Ordejon. “Phonon Dispersion in Graphite”. *Physical Review Letters* **92**, 075501 (2004)
- [Met10] C. Metzger, S. Remi, M. Liu, S. V. Kusminskiy, A. H. C. Neto, A. K. Swan, B. B. Goldberg. “Biaxial Strain in Graphene Adhered to Shallow Depressions”. *Nano Letters* **10**, 6–10 (2010)
- [Mia12] X. Miao, S. Tongay, M. K. Petterson, K. Berke, A. G. Rinzler, B. R. Appleton, A. F. Hebard. “High Efficiency Graphene Solar Cells by Chemical Doping”. *Nano Letters* **12**, 2745–2750 (2012)
- [Nai08] R. R. Nai, P. Blake, A. N. Grigorenko, K. S. Novoselov, T. J. Booth, T. Stauber, N. M. R. Peres, A. K. Geim. “Fine Structure Constant Defines Visual Transparency of Graphene”. *Science* **320**, 1308 (2008)
- [Nai10] R. R. Nair, P. Blake, J. R. Blake, R. Zan, S. Anissimova, U. Bangert, A. P. Golovanov, S. V. Morozov, A. K. Geim, K. S. Novoselov, T. Latychevskaia. “Graphene as a transparent conductive support for studying biological molecules by transmission electron microscopy”. *Applied Physics Letters* **97**, 153102 (2010)
- [Nak96] K. Nakada, M. Fujita, G. Dresselhaus, M. S. Dresselhaus. “Edge state in graphene ribbons: Nanometer size effect and edge shape dependence”. *Physical Review B* **54**, 17954–17961 (1996)

- [Nar08] R. Narula, S. Reich. “Double resonant Raman spectra in graphene and graphite: A two-dimensional explanation of the Raman amplitude”. *Physical Review B* **78**, 165422 (2008)
- [Net07] A. H. C. Neto, F. Guinea. “Electron-phonon coupling and Raman spectroscopy in graphene”. *Physical Review B* **75**, 045404 (2007)
- [Ni08a] Z. Ni, Y. Wang, T. Yu, Y. You, Z. Shen. “Reduction of Fermi velocity in folded graphene observed by resonance Raman spectroscopy”. *Physical Review B* **77**, 235403 (2008)
- [Ni08b] Z. H. Ni, T. Yu, Y. H. Lu, Y. Y. Wang, Y. P. Feng, Z. X. Shen. “Uniaxial Strain on Graphene: Raman Spectroscopy Study and Band-Gap Opening”. *ACS Nano* **2**, 2301–2305 (2008)
- [NI10] P. Nemes-Incze, G. Magda, K. Kamaràs, L. Biró, K. v. Klitzing, J. H. Smet. “Crystallographically Selective Nanopatterning of Graphene on SiO₂”. *Nano Research* **3**, 110–116 (2010)
- [Nik12] A. Y. Nikitin, F. Guinea, L. Martin-Moreno. “Resonant plasmonic effects in periodic graphene antidot arrays”. *Applied Physics Letters* **101**, 151119 (2012)
- [Nov04] K. S. Novoselov, A. K. Geim, S. V. Morozov, D. Jiang, Y. Zhang, S. V. Dubonos, I. V. Grigorieva, A. A. Firsov. “Electric Field Effect in Atomically Thin Carbon Films”. *Science* **306**, 666–669 (2004)
- [Nov05] K. S. Novoselov, D. Jiang, F. Schedin, T. J. Booth, V. V. Khotkevich, S. V. Morozov, A. K. Geim. “Two-dimensional atomic crystals”. *Proceedings of the National Academy of Sciences of the United States of America* **102**, 10451–10453 (2005)
- [Obe13] F. Oberhuber, S. Blien, S. Heydrich, F. Yaghobian, T. Korn, C. Schüller, C. Strunk, D. Weiss, J. Eroms. “Weak localization and Raman study of anisotropically etched graphene antidots”. *Applied Physics Letters* **103**, 143111 (2013)
- [Oht06] T. Ohta, A. Bostwick, T. Seyller, K. Horn, E. Rotenberg. “Controlling the electronic structure of bilayer graphene”. *Science* **313**, 951–954 (2006)
- [Ouy11] F. Ouyang, S. Peng, Z. Liu, Z. Liu. “Bandgap Opening in Graphene Antidot Lattices: The Missing Half”. *ACS Nano* **5**, 4023–4030 (2011)
- [Par06] B. Partoens, F. M. Peeters. “From graphene to graphite: Electronic structure around the K point”. *Physical Review B* **74**, 075404 (2006)
- [Ped08] T. G. Pedersen, C. Flindt, J. Pedersen, N. A. Mortensen, A.-P. Jauho, K. Pedersen. “Graphene Antidot Lattices: Designed Defects and Spin Qubits”. *Physical Review Letters* **100**, 136804 (2008)

- [Pei35] R. Peierls. “Quelques propriétés typiques des corps solides”. *Annales de l’Institut H. Poincaré* **5**, 177–222 (1935)
- [Per06] N. M. R. Peres, F. Guinea, A. H. C. Neto. “Electronic properties of disordered two-dimensional carbon”. *Physical Review B* **73**, 125411 (2006)
- [Pet11] R. Petersen, R. G. Pedersen, A.-P. Jauho. “Clar Sextet Analysis of Triangular, Rectangular, and Honeycomb Graphene Antidot Lattices”. *ACS Nano* **5**, 523–529 (2011)
- [Pim07] M. A. Pimenta, G. Dresselhaus, M. S. Dresselhaus, L. G. Cançado, A. Jorio, R. Saito. “Studying disorder in graphite-based systems by Raman spectroscopy”. *Physical Chemistry Chemical Physics* **9**, 1276–1290 (2007)
- [Pis04] S. Piscanec, M. Lazzeri, F. Mauri, A. C. Ferrari, J. Robertson. “Kohn Anomalies and Electron-Phonon Interactions in Graphite”. *Physical Review Letters* **93**, 185503 (2004)
- [Pis07] S. Pisana, M. Lazzeri, C. Casiraghi, K. S. Novoselov, A. K. Geim, A. C. Ferrari, F. Mauri. “Breakdown of the adiabatic Born-Oppenheimer approximation in graphene”. *Nature Materials* **6**, 198–201 (2007)
- [Ple12a] G. Plechinger, S. Heydrich, J. Eroms, D. Weiss, C. Schüller, T. Korn. “Raman spectroscopy of the interlayer shear mode in few-layer MoS₂ flakes”. *Applied Physics Letters* **101**, 101906 (2012)
- [Ple12b] G. Plechinger, F.-X. Schrettenbrunner, J. Eroms, D. Weiss, C. Schüller, T. Korn. “Low-temperature photoluminescence of oxide-covered single-layer MoS₂”. *Physica Status Solidi Rapid Research Letters* **6**, 126 (2012)
- [Pon05] W.-T. Pong, C. Durkan. “A review and outlook for an anomaly of scanning tunnelling microscopy (stm): superlattices on graphite”. *Journal of Physics D: Applied Physics* **38**, 329–355 (2005)
- [Pop11] D. Popa, Z. Sun, T. Hasan, F. Torrisi, F. Wang, A. C. Ferrari. “Graphene Q-switched, tunable fiber laser”. *Applied Physics Letters* **98**, 073106 (2011)
- [Rad11] B. Radisavljevic, A. Radenovic, J. Brivio, V. Giacometti, A. Kis. “Single-layer MoS₂ transistors”. *Nature Nanotechnology* **6**, 147–150 (2011)
- [Ram28] C. V. Raman, K. S. Krishnan. “A new type of secondary radiation”. *Nature* **121**, 501–502 (1928)
- [Rei02] S. Reich, J. Maultzsch, C. Thomsen, P. Ordejon. “Tight-binding description of graphene”. *Physical Review B* **66**, 035412 (2002)
- [Rei04] S. Reich, C. Thomsen. “Raman spectroscopy of graphite”. *Philosophical Transactions of the Royal Society of London A* **362**, 2271–2288 (2004)

- [Sai02] R. Saito, A. Jorio, A. G. S. Filho, G. Dresselhaus, M. S. Dresselhaus, M. A. Pimenta. “Probing Phonon Dispersion Relations of Graphite by Double Resonance Raman Scattering”. *Physical Review Letters* **88**, 027401 (2002)
- [Shi11] Z. Shi, R. Yang, L. Zhang, Y. Wang, D. Liu, D. Shi, E. Wang, G. Zhang. “Patterning Graphene with Zigzag Edges by Self-Aligned Anisotropic Etching”. *Advanced Materials* **23**, 3061–3065 (2011)
- [Slo58] J. C. Slonczewski, P. R. Weiss. “Band Structure of Graphite”. *Physical Review* **109**, 272–279 (1958)
- [Sme23] A. Smekal. “Zur Quantentheorie der Dispersion”. *Naturwissenschaften* **11**, 873–875 (1923)
- [Son06a] Y.-W. Son, M. L. Cohen, S. G. Louie. “Energy Gaps in Graphene Nanoribbons”. *Physical Review Letters* **97**, 216803 (2006)
- [Son06b] Y.-W. Son, M. L. Cohen, S. G. Louie. “Half-metallic graphene nanoribbons”. *Nature* **444**, 347–349 (2006)
- [Sta11] J. Stadler, T. Schmid, R. Zenobi. “Nanoscale chemical imaging of single-layer graphene”. *ACS Nano* **5**, 8442–8448 (2011)
- [Sun10] Z. Sun, T. Hasan, F. Torrisi, D. Popa, G. Privitera, F. Wang, F. Bonaccorso, D. M. Basko, A. C. Ferrari. “Graphene Mode-locked Ultrafast Laser”. *ACS Nano* **4**, 803–810 (2010)
- [Tan12] P. H. Tan, W. P. Han, W. J. Zhao, Z. H. Wu, K. Chang, H. Wang, Y. F. Wang, N. Bonini, N. Marzari, N. Pugno, G. Savani, A. Lombardo, A. C. Ferrari. “The shear mode of multilayer graphene”. *Nature Materials* **11**, 294–300 (2012)
- [Tho00] C. Thomsen, S. Reich. “Double Resonant Raman Scattering in Graphite”. *Physical Review Letters* **85**, 5214–5217 (2000)
- [Tia94] W. Tian, S. Datta. “Aharonov-Bohm-type effect in graphene tubules: A Landauer approach”. *Physical Review B* **49**, 5097–5100 (1994)
- [Tui70] F. Tuinstra, J. L. Koenig. “Raman spectrum of graphite”. *Journal of Chemical Physics* **53**, 1126 (1970)
- [Ven11] P. Venezuela, M. Lazzeri, F. Mauri. “Theory of double-resonant Raman spectra in graphene: Intensity and line shape of defect-induced and two-phonon bands”. *Physical Review B* **84**, 035433 (2011)
- [Wal47] P. R. Wallace. “The Band Theory of Graphite”. *Physical Review* **71**, 622–635 (1947)
- [Wan08] X. Wang, L. Zhi, K. Müllen. “Transparent, Conductive Graphene Electrodes for Dye-Sensitized Solar Cells”. *Nano Letters* **8**, 323–327 (2008)

- [Wei91] D. Weiss, M. L. Roukes, A. Menschig, P. Grambow, K. von Klitzing, G. Weimann. “Electron Pinball and Commensurate Orbits in a Periodic Array of Scatterers”. *Physical Review Letters* **66**, 21 (1991)
- [Wei94] D. Weiss, K. Richter, E. Vasiliadou, G. Lütjering. “Magnetotransport in antidot arrays”. *Surface Science* **305**, 408–418 (1994)
- [Wim08] M. Wimmer, I. Adagideli, S. Berber, D. Tománek, K. Richter. “Spin Currents in Rough Graphene Nanoribbon: Universal Fluctuations and Spin Injection”. *Physical Review Letters* **100**, 177207 (2008)
- [Woo00] L. M. Woods, G. D. Mahan. “Electron-phonon effects in graphene and arm-chair (10,10) single-wall carbon nanotubes”. *Phys. Rev. B* **61**, 10651–10663 (2000)
- [Wu10] Y. Wu, Y. m. Lin, A. A. Bol, K. A. Jenkins, F. Xia, D. B. D. B. F. Zhu, P. Avouris. “High-frequency, scaled graphene transistors on diamond-like carbon”. *Nature* **472**, 74–78 (2010)
- [Xia09] F. Xia, T. Mueller, Y. M. Lin, A. Valdes-Garcia, P. Avouris. “Ultrafast graphene photodetector”. *Nature Nanotechnology* **4**, 839–843 (2009)
- [Yag12] F. Yaghobian, T. Korn, C. Schüller. “Frequency Shift in Graphene-Enhanced Raman Signal of Molecules”. *ChemPhysChem* **13**, 4271–4275 (2012)
- [Yan07] J. Yan, Y. Zhang, P. Kim, A. Pinczuk. “Electric Field Effect Tuning of Electron-Phonon Coupling in Graphene”. *Physical Review Letters* **98**, 166802 (2007)
- [Yan10] R. Yang, L. Zhang, Y. Wang, Z. Shi, D. Shi, H. Gao, E. Wang, G. Zhang. “An Anisotropic Etching Effect in the Graphene Basal Plane”. *Advanced Materials* **22**, 4014–4019 (2010)
- [Yaz08] O. V. Yazyev, M. I. Katnelson. “Magnetic Correlations at Graphene Edges: Basis for Novel Spintronics Devices”. *Physical Review Letters* **100**, 048209 (2008)
- [Yoo09] D. Yoon, H. Moon, Y.-W. Son, J. S. Choi, B. H. Park, Y. H. Cha, Y. D. Kim, H. Cheong. “Interference effect on Raman spectrum of graphene on SiO_2/Si ”. *Physical Review B* **80**, 125422 (2009)
- [You08] Y. You, Z. Ni, T. Yu, Z. Shen. “Edge chirality determination of graphene by Raman spectroscopy”. *Applied Physics Letters* **93**, 163112 (2008)
- [Zha10] H. Zhang, D. Tang, R. J. Knize, L. Zhao, Q. Bao, K. P. Loh. “Graphene mode locked, wavelength-tunable, dissipative soliton fiber laser”. *Applied Physics Letters* **96**, 111112 (2010)

- [Zha13] X. Zhang, O. V. Yazyev, J. Feng, L. Xie, C. Tao, Y.-C. Chen, L. Jiao, Z. Pe-dramrazi, A. Zettl, S. G. Louie, H. Dai, M. F. Crommie. “Experimentally engineering the edge termination of graphene nanoribbons”. *ACS Nano* **7**, 198–202 (2013)
- [Zho07] S. Y. Zhou, G.-H. Gweon, A. V. Fedorov, P. N. First, W. A. de Heer, D.-H. Lee, F. Guinea, A. H. C. Neto, A. Lanzara. “Substrate-induced bandgap opening in epitaxial graphene”. *Nature Materials* **6**, 770–775 (2007)
- [Zhu13] X. Zhu, W. Wang, W. Yan, M. B. Larsen, P. Bøggild, T. G. Pedersen, S. Xiao, J. Zi, N. A. Mortensen. “Plasmon-phonon coupling in large-area graphene dot and antidot arrays”. *arXiv* **1312**, 2400v1 (2013)

Danksagung

Mein herzlicher Dank gilt Allen, die zum Gelingen dieser Arbeit beigetragen haben. Besonders danken möchte ich:

- Prof. Dr. Christian Schüller, der die Arbeit angeleitet hat, mir immer mit Rat zur Seite stand, mir ermöglichte, an vielen Tagungen teilzunehmen und in professioneller Hinsicht immer ein ausgezeichnetes Vorbild war.
- PD Dr. Tobias Korn für tatkräftige Unterstützung im Labor und außerhalb, für eine Vielzahl nützlicher Ratschläge und - nicht zuletzt- fürs Korrekturlesen dieser Arbeit.
- Christof Ermer für technische Unterstützung und viele nützliche kleine Gadgets fürs Labor.
- Florian Oberhuber und Jonathan Eroms für das Bereitstellen von Proben und generell professionelle Zusammenarbeit.
- meinen Büro-Mit-Insassen Michael Hirmer und Mike Kugler für die angenehme Gesellschaft und dem Rest der AG Schüller für die kollegiale Zusammenarbeit und eine schöne Zeit.
- Meinen Eltern, Andi und Michael.

Erklärung

Hiermit erkläre ich, dass ich die vorliegende Arbeit selbstständig angefertigt und keine Hilfsmittel außer den in der Arbeit angegebenen benutzt habe.

Regensburg, den